AIP | Physics of Fluids

Simulation-based study of wind loads on semi-submersed object in ocean wave field

Shengbai Xie, Di Yang, Yi Liu, and Lian Shen

Citation: Physics of Fluids **28**, 015106 (2016); doi: 10.1063/1.4939271
View online: http://dx.doi.org/10.1063/1.4939271
View Table of Contents: http://scitation.aip.org/content/aip/journal/pof2/28/1?ver=pdfcov
Published by the AIP Publishing

Articles you may be interested in

Numerical simulation of Faraday waves oscillated by two-frequency forcing
Phys. Fluids **27**, 032108 (2015); 10.1063/1.4915340

Flow past a normal flat plate undergoing inline oscillations
Phys. Fluids **24**, 093603 (2012); 10.1063/1.4749803

Hydroelastic response and energy harvesting potential of flexible piezoelectric beams in viscous flow
Phys. Fluids **24**, 054106 (2012); 10.1063/1.4719704

Structure formation in the oceanic subsurface bubble layer by an internal wave field
Phys. Fluids **22**, 106603 (2010); 10.1063/1.3499379

The existence of vortices in the wakes of simulated raindrops
Phys. Fluids **17**, 031706 (2005); 10.1063/1.1874192

This article is copyrighted as indicated in the article. Reuse of AIP content is subject to the terms at: http://scitation.aip.org/termsconditions. Downloaded to IP: 129.7.106.213 On: Tue, 19 Jan 2016 17:21:50

CrossMark click for updates

PHYSICS OF FLUIDS **28**, 015106 (2016)

Simulation-based study of wind loads on semi-submersed object in ocean wave field

Shengbai Xie,[1] Di Yang,[2] Yi Liu,[3] and Lian Shen[4,5,a)]
[1]*College of Earth, Ocean, and Environment, University of Delaware, Newark, Delaware 19716, USA*
[2]*Department of Mechanical Engineering, University of Houston, Houston, Texas 77204, USA*
[3]*Department of Civil Engineering, Johns Hopkins University, Baltimore, Maryland 21218, USA*
[4]*Department of Mechanical Engineering, University of Minnesota, Minneapolis, Minnesota 55455, USA*
[5]*St. Anthony Falls Laboratory, University of Minnesota, Minneapolis, Minnesota 55414, USA*

(Received 26 September 2015; accepted 17 December 2015; published online 15 January 2016)

Wind forcing makes a vital contribution to the hydrodynamic loads on structures at sea. The flow physics is complex, involving interactions among surface water waves, turbulent wind, and semi-submersed object. We perform a simulation-based study on a canonical problem of wind past a semi-submersed rectangular prism with the focus on the wave effect, which is an essential factor in wind loads at sea but has been elusive. To tackle this problem, we develop a hybrid simulation method consisting of two parts: a precursor simulation of coupled wind and wave motions in the far field upstream to provide physical inflow condition, and a near-field simulation of the air and water motions around the object. The simulation method is validated through numerical tests and comparisons with data from the literature for different aspects of the code. This hybrid simulation method is then applied to study the effect of surface wave motions on the wind load on the object. Various wave conditions are considered, including pure wind-sea satisfying the Joint North Sea Wave Project spectrum as well as wind-sea mixed with long-wavelength ocean swells. The simulation results exhibit significant oscillations in the wind load on the object. The oscillations are found to correlate well with the incident wave motions and are particularly strong in the presence of swells. The underlying mechanism is explained through analyses on variations of wind speed with different wave phases and wave-correlated flow patterns of the wind when it impinges on the object. Our simulations also indicate that waves have an appreciable effect on the wake behind the object. © *2016 AIP Publishing LLC.* [http://dx.doi.org/10.1063/1.4939271]

I. INTRODUCTION

The wind effect on semi-submersed objects in oceanic wave field is important for many applications. Wind load can strongly affect the operation and safety of ships and offshore structures,[1,2] making it an important factor in naval architecture and ocean engineering.[3] Recent studies on offshore wind energy have shown that ocean waves can have an appreciable impact on the lower part of marine atmospheric boundary layer, resulting in wave-correlated variation in the power output of offshore wind farms.[4,5] From the viewpoint of fundamental fluid mechanics, this is an interesting and profound problem involving complex interactions among wind turbulence, water waves, and structures.

a)Author to whom correspondence should be addressed. Electronic mail: shen@umn.edu.

 ©2016 AIP Publishing LLC

This article is copyrighted as indicated in the article. Reuse of AIP content is subject to the terms at: http://scitation.aip.org/termsconditions. Downloaded to IP: 129.7.106.213 On: Tue, 19 Jan 2016 17:21:50

In the past, great efforts have been devoted to the study of flows past obstacles mounted on rigid ground in the context of wind engineering for buildings and structures. For example, Baines[6] performed wind-tunnel experiments to study the surface pressure distribution on model buildings. Wind-tunnel measurements by Castro and Robins[7] indicated that the surface pressure on a ground-mounted cube and the velocity in the wake fluctuate significantly with both uniform and sheared turbulent inflows. A full-scale field measurement by Richards *et al.*[8] showed that the roof and leeward wall pressures vary in response to the characteristics of incoming winds, e.g., velocity profile, turbulence intensity, etc. Theoretically, Hunt *et al.*[9] revealed several key features of flow patterns around the object, including nodes and saddles, based on the kinematical theory. Numerically, Murakami *et al.*[10,11] used large-eddy simulation (LES) to study details of winds around a ground-mounted bluff body as well as aerodynamic pressure on the body surface.

With the knowledge learned from the rigid-surface studies, traditionally, the wind loads on offshore structures and marine vessels were evaluated based on land-mounted structures but with modifications pertaining to ocean conditions, e.g., reduced surface roughness height.[3] Various models have been proposed for evaluations of wind pressure forces and moments using flat-ground wind-tunnel measurements that mimic smooth ocean surface.[12,13] While some successes have been achieved in naval applications by using such simplified models, the dynamic effect of surface waves by their motions has been completely omitted. The moving, curved sea surface due to waves adds substantial complexities to the air flow, through the kinematic constraint and dynamic distortion of the wavy air–sea interface on the turbulent wind.

Previous studies have shown that wind turbulence above the sea exhibits important and distinct characteristics compared to that over a flat stationary surface, because of the moving wave surface.[14,15] As revealed by direct numerical simulations (DNSs) of turbulent flows over idealized progressive waves,[16,18,19] the turbulence properties are strongly dependent on wave characteristics including the wave propagation speed and wave steepness. Previous studies have shown that the wave-induced disturbance in the velocity and pressure of the air flow can extend vertically to an elevation of the order of wavelength.[16,18–21] Therefore, long waves in the oceans such as swells, which have wavelengths of $O(100)$ m, can have a significant effect on the lower marine atmospheric boundary layer. By using LES to study wind turbulence above prescribed and fast propagating swells, Sullivan *et al.*[21] showed that the turbulence production mechanism is modified by the momentum transfer from the ocean to the wind, and the near-surface wind speed is high above the wave troughs of the swells and low above the crests. Yang and Shen[22] developed a wind–wave coupled simulation method, which dynamically couples a DNS of wind turbulence with a potential-flow-based simulation of nonlinear water waves. As such, the evolution of waves due to wind forcing and the feedback of wave motions on the wind are both captured. Recently, the turbulence solver in this coupled method has been extended from DNS to LES to address the high Reynolds numbers of atmospheric boundary layer flows.

Due to its importance in marine applications, the problem of flows past semi-submersed structures has received increasing attention in recent years. There were a number of studies performed with different focuses. For example, laboratory experiments with semi-submersed cylinders have revealed details of the wake flow in water.[24–26] In a LES-based study, Kawamura *et al.*[27] examined the effect of Froude number on interactions between waves and wakes. The effect of free surface on vortices in the near wake and loads on the cylinders were studied by Yu *et al.*[28] The mechanism of vortex shedding and interactions of vortices with the free surface was investigated by Suh *et al.*[29] Most of the studies focused on flows on the water side, and incident wind-generated waves were usually not considered. Wind loads and the distortion effect of waves on the air flow remain elusive, which motivate the current work.

The objective of this work is to develop a computational approach that can address wind and wave coupling and provide details of air and water flows around semi-submersed structures and to use simulations to quantify the effect of waves on the wind loads. We aim to overcome some of the limitations in previous studies, such as neglecting wave effects on the wind and simplifying the wind inflow as uniform. We consider a rectangular prism that is semi-submersed and stationary, which serves as a canonical problem representative of the surface-piercing part of a stiffly moored offshore structure, such as an oil drilling tension-leg platform or the platform of an offshore wind

This article is copyrighted as indicated in the article. Reuse of AIP content is subject to the terms at: http://scitation.aip.org/termsconditions. Downloaded to IP: 129.7.106.213 On: Tue, 19 Jan 2016 17:21:50

turbine attached to seabed by high-tension cables.[30,31] This idealized and canonical problem setup allows us to focus on understanding the effect of coupled wind–wave motions on the wind load. We remark that more complex flow–structure interaction phenomena would occur if one considers floating objects with loose mooring system that allows considerable floating motions.

Our computations consist of two parts: (a) a far-field simulation that couples the simulation of nonlinear wave field using a high-order spectral method (HOSM) and the simulation of wind using LES on wave-surface-fitted grid, which is pre-calculated to generate inflow condition that feeds to (b) a near-field simulation to capture the flow–structure interaction around a semi-submersed object. In particular, in the near-field simulation, the air–water two-fluid flow system is modeled by a level-set method, with a signed distance function for tracking the air–water interface;[33–35] the presence of the semi-submersed object is modeled using an immersed boundary method.[36–38] We note that instead of pre-calculating the precursor simulation to generate inflow condition, Stevens *et al.*[32] developed a concurrent approach to couple and simultaneously carry out the precursor and main simulations that have similar numerical schemes. However, their concurrent approach is not applicable for this study because the numerical schemes for the far-field (precursor) and near-field (main) simulations are very different, which makes the concurrent scheme too complicated to implement. Therefore, we chose to pre-calculate the far field in a way similar to what has been done in many prior LES studies.

To study the effect of ocean surface waves on the wind load on the object, different wave conditions are considered, including local wind waves described by the JONSWAP (Joint North Sea Wave Project) wave spectrum[39] and the mixing of them with swells. Swells are generated by remote storms and propagate to the local region in the form of long crest, long wavelength, high amplitude, and fast traveling waves. Because they can be generated at many locations in the world and decay slowly as propagating to the region of interest, swells are known to play an important role in air–sea interactions.[15,21,40,41] As shown in this paper, waves, especially swells, strongly affect the air flow and the wind loads on the object.

The remainder of this paper is organized as follows: Section II introduces the numerical methods for both the far-field wind–wave coupled simulation and the near-field simulation for air and water flows around the object. Validations of the numerical methods are shown in Section III. Results are presented and discussed in Section IV. Finally, conclusions are made in Section V.

II. NUMERICAL METHODS

As illustrated in Fig. 1, our simulations consist of two parts. In the far field upstream, coupled simulations of wind and wave interactive motions are performed to generate physical inflow conditions for the near-field simulation, which computes the motions of air and water around a semi-submersed object. The detailed numerical methods used in these two parts of simulations are introduced, respectively, in Subsections II A and II B.

A. Simulations of wind and waves in far field

In the far field, LES is performed for the turbulent wind field, and the wave field is simulated based on potential flow theory. The wind and wave fields are dynamically coupled at each time step in the simulation. The numerical methods are briefly described below. More details can be found in Yang and Shen[22,42] and Yang *et al.*[23]

The motion of wind turbulence is described by the filtered Navier–Stokes equations

$$\frac{\partial \widetilde{u}_i}{\partial t} + \widetilde{u}_j \frac{\partial \widetilde{u}_i}{\partial x_j} = -\frac{1}{\rho_a}\frac{\partial \widetilde{p}}{\partial x_i} - \frac{\partial \tau_{ij}^r}{\partial x_j} - \frac{1}{\rho_a}\Pi\delta_{i1}, \tag{1}$$

$$\frac{\partial \widetilde{u}_i}{\partial x_i} = 0, \tag{2}$$

where $i = 1,2,3$, and $\widetilde{(\cdot)}$ denotes a variable resolved by the LES grid. Here, $\widetilde{u}_i$ is the resolved wind velocity; ρ_a is air density; τ_{ij}^r is the trace-free part of the SGS stress tensor; p is the modified

This article is copyrighted as indicated in the article. Reuse of AIP content is subject to the terms at: http://scitation.aip.org/termsconditions. Downloaded to IP: 129.7.106.213 On: Tue, 19 Jan 2016 17:21:50

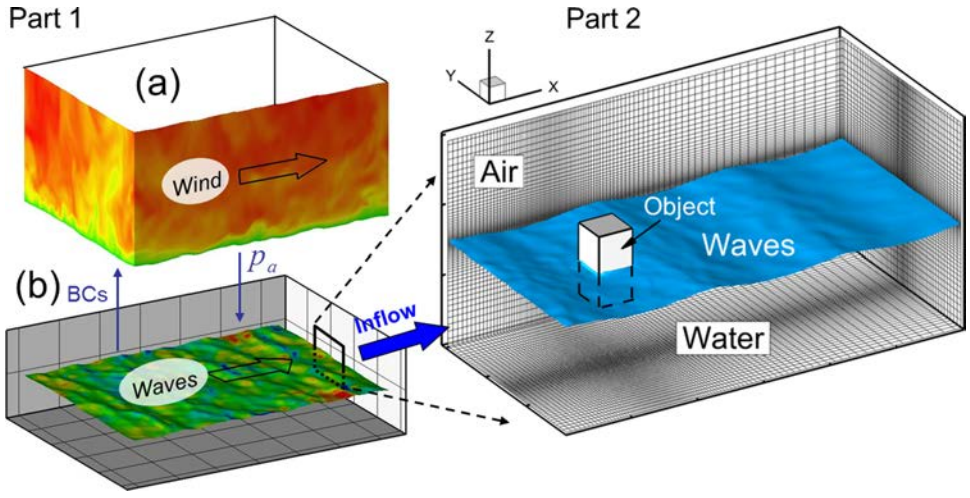

FIG. 1. Illustration of the simulation strategy. Part 1 is the precursor far-field wind and wave coupled simulations, which generates physical inflow conditions for Part 2, the near-field simulation of air and water motions around a semi-submersed object. In Part 1, the upper portion (a) is LES of wind field and the lower portion (b) is HOSM simulation of wave field. The domain (a) is artificially lifted up in the plot for a better visualization of domain (b), in which only the wave surface is shown. In Part 2 the grid lines are plotted on the three representative planes for every two actual computational grid lines used in each direction.

dynamic pressure including the trace of the SGS stress tensor; and δ_{i1} is the Kronecker delta function. The SGS stress tensor τ_{ij}^r is modeled using the Lagrangian-averaged scale-dependent dynamic Smagorinsky model.[44] The air flow is driven by a streamwise pressure gradient Π. For a fully developed, statistically steady air turbulent flow driven by a mean pressure gradient, the corresponding friction velocity is

$$u_* = \sqrt{-\frac{\Pi \overline{H}}{\rho_a}}, \tag{3}$$

where $\overline{H}$ is the mean height of the computational domain of the LES. For the marine–atmospheric boundary layer flow considered in this study, the Reynolds number is sufficiently high ($Re_H = U_H \overline{H}/\nu = O(10^8)$, where U_H is the mean wind velocity at $z = \overline{H}$), for which the molecular viscosity term is neglected similar to many other LES studies of atmospheric boundary layer flows.[43–45]

Similar to many prior LES studies,[43–45] in the far field the simulation of atmospheric boundary layer flow is conducted by considering a pressure-driven half-channel turbulent flow, with zero-stress and zero-penetration conditions for the wall-parallel and wall-normal velocities on the top boundary, respectively. Periodic conditions are used in the streamwise and spanwise directions. The bottom of the air domain is bounded by progressive water waves. A boundary-fitted grid is used for the wind LES to capture the wave effect. The following algebraic mapping,

$$\xi = x, \quad \psi = y, \quad \zeta = \frac{z - \widetilde{\eta}}{\widetilde{H}(x,y,t)} = \frac{z - \widetilde{\eta}(x,y,t)}{\overline{H} - \widetilde{\eta}(x,y,t)}, \quad \tau = t, \tag{4}$$

is used to transfer the irregular wave-surface-bounded air domain in the physical space (x, y, z, t) to a right-rectangular prism in the computational space (ξ, ψ, ζ, τ). Here, the height of the physical domain of air, $\widetilde{H}(x, y, t)$, is decomposed into an average height $\overline{H}$ and a wave induced variation $-\widetilde{\eta}(x, y, t)$, with $\widetilde{\eta}$ being the filtered wave surface elevation.

The air domain is discretized by a pseudo-spectral method in the horizontal directions and a second-order central difference scheme in the vertical direction. A standard logarithmic law-of-the-wall is used to impose the proper sea-surface stress to the LES,[44] with an SGS sea-surface roughness of 2×10^{-4} m for the wind-wave conditions considered in this study, which is consistent with typical observed values and has been used in previous LES of wind over ocean waves in

This article is copyrighted as indicated in the article. Reuse of AIP content is subject to the terms at: http://scitation.aip.org/termsconditions. Downloaded to IP: 129.7.106.213 On: Tue, 19 Jan 2016 17:21:50

the literature.[21,46] The flow field is advanced in time by a fractional-step method, consisting of a prediction step using the second-order Adams–Bashforth method and a correction step based on the standard projection method to enforce the incompressibility constraint.

The motions of the sea-surface waves are simulated by the high-order spectral method, HOSM.[47] The HOSM is based on potential flow theory, which is applicable to the non-breaking surface gravity waves considered in this study.[48] It simulates nonlinear waves using the Zakharov formulation,[49] in which the wave motion is described by the surface elevation $\eta(x,y,t)$ and the surface potential Φ^s. Here, $\Phi^s = \Phi(x,y,z=\eta(x,y,t),t)$ with Φ being the velocity potential (see Fig. 1 for the definition of coordinates). The wave motion is governed by the Laplace equation $\nabla^2\Phi = 0$ as well as the kinematic and dynamic conditions at the sea surface $z = \eta(x,y,t)$,

$$\frac{\partial \eta}{\partial t} + \nabla_h \eta \cdot \nabla_h \Phi^s - (1 + \nabla_h \eta \cdot \nabla_h \eta)\frac{\partial \Phi}{\partial z} = 0, \tag{5}$$

$$\frac{\partial \Phi^s}{\partial t} + g\eta + \frac{1}{2}\nabla_h \Phi^s \cdot \nabla_h \Phi^s + \frac{p_a}{\rho_w} - \frac{1}{2}(1 + \nabla_h \eta \cdot \nabla_h \eta)\left(\frac{\partial \Phi}{\partial z}\right)^2 = 0. \tag{6}$$

Here, $\nabla_h = (\partial/\partial x, \partial/\partial y)$ is the horizontal gradient, g is the gravitational acceleration, p_a is the air pressure at the wave surface, and ρ_w is the density of water.

In HOSM, Eqs. (5) and (6) are decomposed into individual perturbation modes with respect to the wave steepness and further expanded from the actual wave surface to the mean surface elevation using Taylor series expansion. A pseudo-spectral method is employed for spatial discretizations in the horizontal directions. Vertical variations of the variables are taken into account following the wave theory, with the exact formulation chosen according to the water depth condition and bottom topology. The wave field is advanced in time by a fourth-order Runge–Kutta scheme. Details of the numerical implementation of the HOSM are provided in Yang and Shen.[22] A complete review of the HOSM and a collection of its representative applications can be found in Mei *et al.*[48]

The LES of wind and the HOSM simulation of waves are coupled through a fractional-step method with two-way feedback.[22] In the simulation, the wind and wave fields have the same horizontal dimensions. At each time step, the HOSM simulation provides the sea surface geometry and velocity to the wind LES as its bottom boundary conditions for LES to advance to the next time step. From the wind simulation, the air pressure distribution at the wave surface at the new time step is obtained, which generates form drag that is primarily responsible for the momentum and energy transfer between wind and water.[15,46] The HOSM simulation uses this air pressure in dynamic free-surface boundary condition (6) to drive the waves, and the wave simulation advances to the new time step.

The outcome wind and wave velocities of the precursor far-field simulation at its outflow boundary are interpolated from the wave-surface-fitted grid to a Cartesian grid, providing the inflow condition for the main air–water coupled simulation in the near field surrounding the semi-submersed object. This precursor-to-main simulation strategy is sketched in Fig. 1. Details of the near-field simulation is introduced in Subsection II B.

B. Near-field simulation of air and water flows around a semi-submersed object

In the near field surrounding the semi-submersed object, the air and water motions are described by the following filtered Navier–Stokes equations for incompressible multi-phase turbulent flows,

$$\frac{\partial \widetilde{u}_i}{\partial t} = -\widetilde{u}_j\frac{\partial \widetilde{u}_i}{\partial x_j} + \frac{1}{\rho}\Big[-\frac{\partial \widetilde{p}}{\partial x_i} + \frac{\partial}{\partial x_j}(2\mu \widetilde{S}_{ij}) - \rho\frac{\partial \tau^r_{ij}}{\partial x_j} + \sigma\kappa\delta(d)n_i\Big] + G_i + \widetilde{f}_i, \tag{7}$$

$$\frac{\partial \widetilde{u}_i}{\partial x_i} = 0. \tag{8}$$

Here, ρ and μ are, respectively, the density and dynamic viscosity of the fluids, which can be for either air or water; S_{ij} is the strain rate tensor; σ is the surface tension of the air–water interface; κ is the curvature of the interface; n_i is the unit normal vector at the interface pointing from water to air; δ is the Dirac delta function; d is the normal distance to the surface; $G_i = (0,0,g)$, where g is the

This article is copyrighted as indicated in the article. Reuse of AIP content is subject to the terms at: http://scitation.aip.org/termsconditions. Downloaded to IP: 129.7.106.213 On: Tue, 19 Jan 2016 17:21:50

gravitational acceleration; and f_i is a body force per unit mass, which is used to model the presence of the object in the context of the immersed boundary method introduced below. Note that for the large-size object studied in this paper, the molecular viscosity term and the surface tension term are negligibly small compared with other terms in Eq. (7). Here, we simply keep these two terms as that is how our code was originally programmed for general purposes. But one should keep in mind that they are dynamically unimportant for the quantification of wind loads, which is the focus of this study.

Finite difference schemes are used to discretize Eqs. (7) and (8) on a Marker-and-Cell grid. The spatial discretization of the advective term uses a linear combination of a fourth-order WENO scheme[50] and a second-order central difference scheme. Eqs. (7) and (8) are advanced in time by a fractional-step method.[51] First, the momentum equation without the pressure term is integrated in time explicitly by a second-order Runge–Kutta scheme. Then a pressure Poisson equation is solved by a bi-conjugate gradient stabilized (Bi-CGSTAB) method[52,53] to obtain pressure correction satisfying mass conservation.

The SGS stress term τ_{ij}^r in Eq. (7) is modeled by a renormalization group (RNG) method[54–56] as

$$\tau_{ij}^r = -2\frac{\mu^{SGS}}{\rho}\widetilde{S}_{ij}. \tag{9}$$

Here,

$$\mu^{SGS} + \mu = \mu\left[1 + \left(\frac{\mu_s^2(\mu^{SGS}+\mu)}{\mu^3} - C\right)\cdot H\left(\frac{\mu_s^2(\mu^{SGS}+\mu)}{\mu^3} - C\right)\right]^{1/3}, \tag{10}$$

where $H(x)$ is the Heaviside step function, defined as $H(x) = 1$ if $x > 0$ and $H(x) = 0$ otherwise; $\mu_s = \rho(c_s\Delta)^2\sqrt{2\widetilde{S}_{ij}\widetilde{S}_{ij}}$, where the Smagorinsky coefficient $c_s = 0.0787$ as suggested by Yakhot *et al.*,[55] and the filter width $\Delta = (\Delta_x\Delta_y\Delta_z)^{1/3}$ with Δ_x, Δ_y, and Δ_z being the local grid sizes in x-, y-, and z-directions, respectively; and C is a constant set to be 75.[54] This model has been found to perform well in studies of multiphase flows reported in the literature and our previous simulation of breaking waves.[57,58]

The phases of air and water are distinguished on a fixed Cartesian grid by a level-set method.[33–35] A level-set function ϕ (also known as the signed distance function) is defined based on the minimum distance to the interface, D, as

$$\phi(\mathbf{x}) = \begin{cases} D & \text{in water} \\ -D & \text{in air} \end{cases}. \tag{11}$$

The air–water interface is represented by the zeroth level of ϕ. The density ρ and viscosity μ in Eq. (7) are expressed as

$$\rho(\phi) = \rho_a(1 - H(\phi)) + \rho_w H(\phi), \tag{12}$$

$$\mu(\phi) = \mu_a(1 - H(\phi)) + \mu_w H(\phi). \tag{13}$$

Here, ρ_a and μ_a are, respectively, the density and viscosity of air, and ρ_w and μ_w are, respectively, the density and viscosity of water. The evolution of ϕ is obtained by solving an advection equation

$$\frac{\partial\phi}{\partial t} + \widetilde{\mathbf{u}}\cdot\nabla\phi = 0. \tag{14}$$

Because the property of ϕ of being a signed distance may not be preserved in time, i.e., the Euclidean norm $|\nabla\phi|$ no longer equals to 1 as the time evolves, the following reinitialization procedure[34] is used as a correction without changing the position of the zeroth level,

$$\frac{\partial\phi_c}{\partial t^*} + \text{sign}(\phi)(|\nabla\phi_c| - 1) = 0. \tag{15}$$

Here, ϕ_c is the corrected function of ϕ and t^* is the artificial time. The steady-state solution of Eq. (15) yields the desired distance function. Using the level-set method, the multi-phase flows of air and water are treated in a fully coupled manner and the air–water interface is traced implicitly and dynamically.

This article is copyrighted as indicated in the article. Reuse of AIP content is subject to the terms at: http://scitation.aip.org/termsconditions. Downloaded to IP: 129.7.106.213 On: Tue, 19 Jan 2016 17:21:50

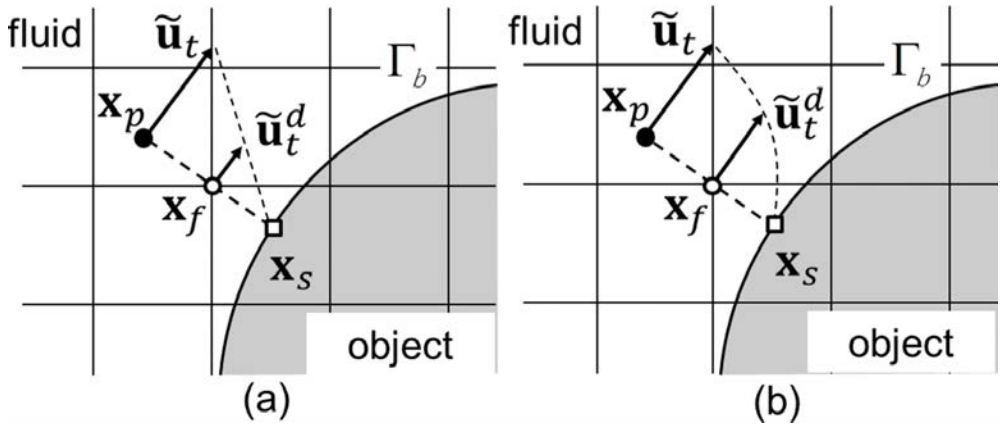

FIG. 2. Sketch of the immersed boundary method (a) without the wall-layer modeling, and (b) with the wall-layer modeling. The filled circle denotes the probe point, the hollow circle denotes the forcing point, and the hollow square denotes the projection point on the surface. The grey shadow zone represents the inner regime of the object, and Γ_b is the surface of the object.

To model the effect of the object, we employ an immersed boundary (IB) method.[38] Here, a series of body forces $\widetilde{f}_i$ on the Cartesian grid points adjacent to the solid surfaces are applied to satisfy the velocity boundary condition at the solid surfaces. The discrete approach of the IB method[38] is used here for the capture of sharp boundaries. In particular, referring to Fig. 2, the calculation and distribution of $\widetilde{f}_i$ are briefly described below.

First, fluid grid points immediately outside of the object are tagged and denoted as the forcing points $\mathbf{x}_f$. The points inside the object are denoted as inner points. Second, the desired velocities $\widetilde{u}_i^d$ at the forcing points and inner points are calculated. For high Reynolds number flows, the standard linear interpolation shown in Fig. 2(a) is not applicable at the forcing points. Therefore, a wall-layer modeling treatment is required to impose the no-slip boundary condition for velocity properly. As shown in Fig. 2(b), for a forcing point $\mathbf{x}_f$, its normal projection point $\mathbf{x}_s$ on the object surface Γ_b is found together with a probe point $\mathbf{x}_p$ along the outward normal direction with the same distance. The velocity $\widetilde{\mathbf{u}}_p$ at $\mathbf{x}_p$ is interpolated from its surrounding flow points because they are less affected by the surface. Then $\widetilde{\mathbf{u}}_p$ is decomposed into a normal component $\widetilde{\mathbf{u}}_n$ and a tangential component $\widetilde{\mathbf{u}}_t$. The kinematic wall shear stress τ_w based on $\widetilde{\mathbf{u}}_t$ is estimated by the Werner–Wengle model[59,60] as

$$|\boldsymbol{\tau}_w| = \begin{cases} \dfrac{2\mu|\widetilde{\mathbf{u}}_t|}{\rho d_p} & \text{if} \quad |\widetilde{\mathbf{u}}_t| \leqslant \dfrac{\mu}{2\rho d_p} A^{\frac{2}{1-B}}, \\ \left[\dfrac{1-B}{2} A^{(1+B)/(1-B)} \left(\dfrac{\mu}{\rho d_p}\right)^{1+B} + \dfrac{1+B}{A} \left(\dfrac{\mu}{\rho d_p}\right)^{B} |\widetilde{\mathbf{u}}_t|\right]^{2/(1+B)} & \text{otherwise}, \end{cases} \tag{16}$$

where $A = 8.3$, $B = 1/7$, and d_p is the distance from the surface to $\mathbf{x}_p$. This wall-layer model was designed to treat points both inside the viscous sub-layer and in the inertial sub-layer, according to the magnitude of $\widetilde{\mathbf{u}}_t$. In other words, it converges to the linear profile for the points inside the viscous sub-layer and the power law for the points outside. Once $\boldsymbol{\tau}_w$ is obtained, the tangential velocity component at the forcing point $\mathbf{x}_f$ can be calculated from the inverse expressions of (16) with d_p replaced by d_f. The normal velocity component at $\mathbf{x}_f$ is calculated by linear interpolation. The desired velocities at the inner points are all set to zero. The forcing term $\widetilde{f}_i$ at time step n is calculated at the forcing points and inner points by

$$\widetilde{f}_i^n = \frac{\widetilde{u}_i^d - \widetilde{u}_i^n}{\Delta t} - RHS_i^n, \tag{17}$$

where Δt is the time step and RHS_i^n is the discretized form of the right hand side of Eq. (7) without the forcing term.

This article is copyrighted as indicated in the article. Reuse of AIP content is subject to the terms at: http://scitation.aip.org/termsconditions. Downloaded to IP: 129.7.106.213 On: Tue, 19 Jan 2016 17:21:50

III. TEST AND VALIDATION

Because of the complexity of the problem, laboratory and field experiments of wind and waves past a semi-submersed object are challenging. As a result, direct comparison or validation of our simulation is infeasible due to the lack of measurement data. Nevertheless, we have performed extensive tests and validations for different aspects of our simulation using the corresponding measurement data for canonical and simplified problems reported in the literature and theoretical results available. Three representative test cases are presented below. First, turbulent wind over a wave field is simulated to test the coupled LES–HOSM approach for the precursor far-field calculation. Next, a decaying wave is simulated to test the level-set method. Finally, a boundary layer flow over a ground-mounted cube is simulated to test the immersed boundary method.

A. Turbulent wind over wave field

The simulation of wind and wave fields in the far field is crucial to providing physical inflow conditions to the near-field simulation of air and water motions surrounding the object. Here, a turbulent wind field is simulated over a wave field that has the JONSWAP spectrum[39] as

$$S(\omega) = \frac{\alpha g^2}{\omega} \exp\left[-\frac{4}{5}\left(\frac{\omega_p}{\omega}\right)^4 \right] \gamma^r, \tag{18}$$

with

$$r = \exp\left[-\frac{(\omega - \omega_p)^2}{2\zeta^2 \omega_p^2} \right]. \tag{19}$$

Here,

$$\alpha = 0.076\left(\frac{U_{10}^2}{Fg}\right)^{0.22}, \quad \omega_p = 22\left(\frac{g^2}{U_{10}F}\right), \quad \gamma = 3.3, \quad \zeta = \begin{cases} 0.07 & \text{if} \quad \omega \le \omega_p \\ 0.09 & \text{if} \quad \omega > \omega_p \end{cases}, \tag{20}$$

where ω is the angular frequency, ω_p is the angular frequency at the spectrum peak, U_{10} is the mean wind speed at the height of 10 m above the sea surface, and F is the fetch. Here, $U_{10} = 9.5$ m/s and $F = 112$ km are chosen. The corresponding friction velocity u_* is 0.36 m/s. Under this condition, the wavelength at the spectrum peak is $\lambda_p = 63.3$ m, and the significant wave height is $H_s = 2.18$ m. The wind LES is performed in a domain with the dimensions of 1000 m × 500 m × 500 m in streamwise (x), spanwise (y), and vertical (z) directions, respectively. A grid with $192 \times 128 \times 128$ points is used here. The wave field has the same horizontal size and resolution. Note that the HOSM for the waves does not require a vertical grid. The LES grid resolution used in this study is comparable to or higher than those used in other recent LES studies of marine atmospheric boundary layer flows.[4,5,21]

Figure 3 shows an instantaneous field of wind and waves. The complex structure of turbulence is seen in the wind field, and the waves are irregular with a broadband spectrum. The averaged streamwise velocity spectra of the wind at a variety of heights are plotted in Fig. 4. The spectra are calculated by one-dimensional Fourier transform in the streamwise direction and are averaged in the spanwise direction and in time. The spectra are normalized by u_* and z and are plotted as a function of $k_x z$, where k_x is the wavenumber in the x-direction. Figure 4 shows that the normalized streamwise spectra at different heights collapse. The spectra scale approximately as $k_x^{-5/3}$ for high values of $k_x z$, and as k_x^{-1} for $k_x z < 1.0$. This result is consistent with the finding of Porté-Agel *et al.*[43] Note that if a swell exists in the wave system, a spectral bump may appear at the swell wavenumber.[5]

A common way of checking the performance of wind–wave simulations is to quantify the sea-surface drag on the wind and the energy transfer between the wind and waves. To do this, we transform the surface elevation and the pressure obtained, respectively, from the HOSM simulation and LES to the wavenumber space in a way similar to the calculation of wind velocity spectra introduced above. The air pressure acting on the sea surface is thus decomposed into different wave modes with wavenumber k.

This article is copyrighted as indicated in the article. Reuse of AIP content is subject to the terms at: http://scitation.aip.org/termsconditions. Downloaded to IP: 129.7.106.213 On: Tue, 19 Jan 2016 17:21:50

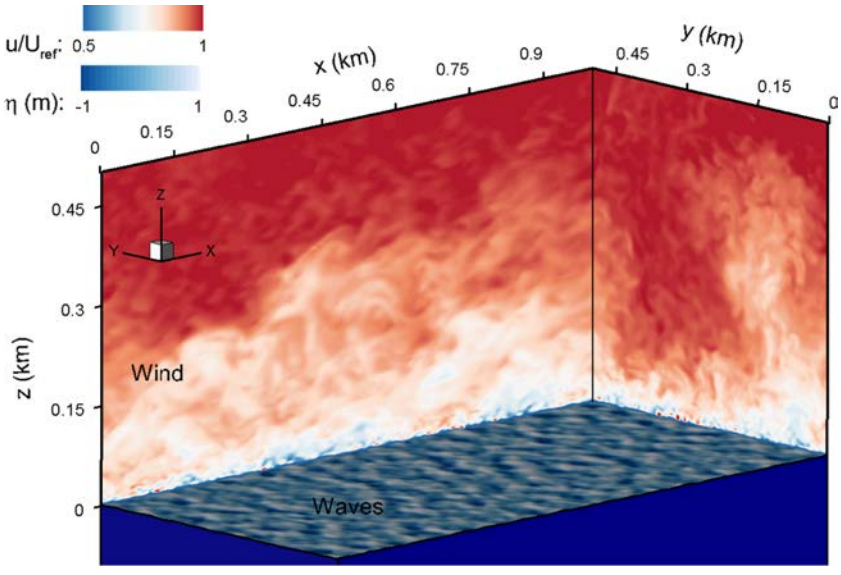

FIG. 3. An instantaneous turbulent wind field above a JONSWAP wave field obtained from the coupled LES–HOSM simulation. The contours of wave surface elevation η are plotted on the water surface, and the contours of streamwise velocity of wind, u, normalized by the mean velocity at the top of the computational domain, U_{ref}, are shown on the two vertical boundaries.

The temporal rate of energy transfer from the wind to the wave mode at wavenumber k is quantified as[61]

$$\gamma(k) = \frac{\rho_w}{\rho_a}\frac{1}{\omega e}\frac{\mathrm{d}e}{\mathrm{d}t} = \left(\frac{u_*}{c}\right)^2 \beta. \tag{21}$$

Here, for the kth mode, $e(k) = \rho_w g[a(k)]^2/2$ is the wave energy density, with $a(k)$ being the corresponding wave amplitude; $\omega = \sqrt{gk}$ is the corresponding angular frequency under deep water condition; β is the wave growth rate parameter,[62] which is related to the wind pressure through[61]

$$\beta(k) = \frac{2}{[a(k)k]^2}\frac{1}{\mathcal{A}}\iint_{\mathcal{A}} \frac{p_k}{\rho_a u_*^2}\frac{\partial \eta_k}{\partial x}\,\mathrm{d}x\mathrm{d}y, \tag{22}$$

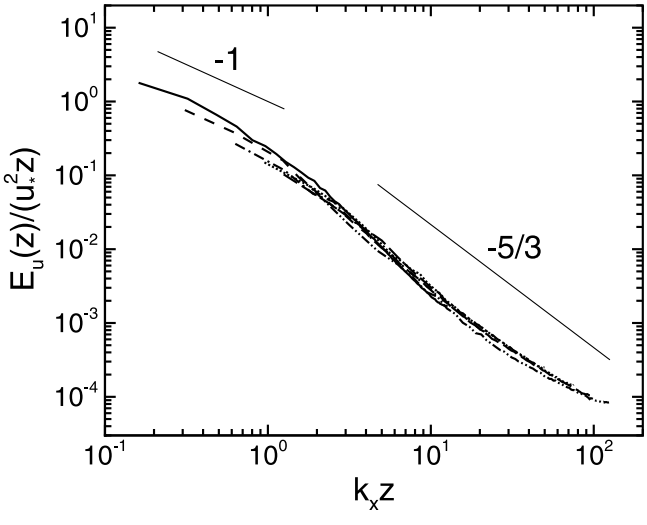

FIG. 4. Normalized streamwise velocity spectra as a function of $k_x z$ for wind turbulence over a JONSWAP wave field obtained from the coupled LES–HOSM simulation. Spectra at different heights are indicated by different lines: ——, $z/\overline{H} = 0.05$; – – –, $z/\overline{H} = 0.1$; – · –, $z/\overline{H} = 0.2$; · · ·, $z/\overline{H} = 0.3$; — —, $z/\overline{H} = 0.4$; and – · · –, $z/\overline{H} = 0.5$.

This article is copyrighted as indicated in the article. Reuse of AIP content is subject to the terms at: http://scitation.aip.org/termsconditions. Downloaded to IP: 129.7.106.213 On: Tue, 19 Jan 2016 17:21:50

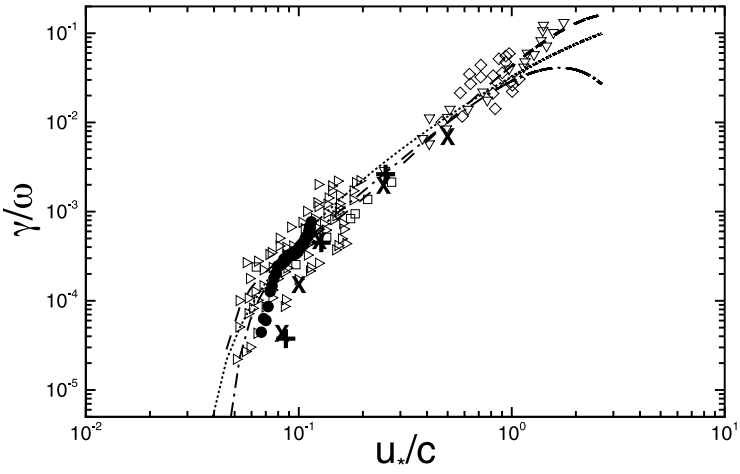

FIG. 5. Dependence of the wave growth rate γ, normalized by angular frequency ω, on the wind–wave velocity ratio u_*/c and comparison of the current LES with previous experiments and simulations. Experimental data compiled by Plant[63] are indicated by open symbols: □, Shemdin and Hsu;[14] ▽, Larson and Wright;[64] ◇, Wu *et al.*;[65] ▷, Snyder *et al.*[66] Values predicted by various wind-wave theories are indicated by lines: −−, Janssen;[67] and − · −, Miles.[62] Values given by the parameterization of Donelan *et al.*[61] are indicated by ⋯. DNS results from Sullivan *et al.*[16] are marked by +. DNS results from Kihara *et al.*[18] are marked by ×. The current LES–HOSM result is indicated by •.

where p_k and η_k are, respectively, the air pressure at the wave surface and the surface displacement for the k-th wave mode, and $\mathcal{A}$ is the surface area. Figure 5 shows the dependence of the dimensionless temporal growth rate of wave, γ/ω, on the wind–wave velocity ratio, u_*/c, i.e., the reciprocal of wave age. Comparison between our simulation result and the data from the literature shows good agreement.

B. Decaying gravity wave

The level-set method adopted in this research has been widely used in previous studies and tested for various free-surface flow problems.[33–35] In order to confirm that it works well in our code, a canonical case of a decaying two-dimensional linear surface gravity wave in deep water is tested, for which an analytical solution is available.[68] In this test, the wave has the surface profile initially as

$$\eta(x, y) = a_0 \cos(kx), \tag{23}$$

with the initial wave velocity field

$$u(x, y, z) = a_0 \omega e^{kz} \cos(kx), \quad v(x, y, z) = 0, \quad w(x, y, z) = a_0 \omega e^{kz} \sin(kx). \tag{24}$$

Here, a_0 is the initial wave amplitude, and $\omega = \sqrt{gk}$ is the angular frequency according to the deep-water wave dispersion relation. The initial wave steepness is set to be $a_0 k = 0.1$. The wave Reynolds number is $\mathrm{Re}_w = ck^{-1}/\nu = 100$, where $c = \sqrt{g/k}$ is the wave phase speed. Consistent with the assumption in Lamb,[68] the surface tension is set to be zero in this test. The initial condition for the air flow is constructed by letting the velocity decay exponentially with height with respect to the wave orbital velocity at the surface according to the potential flow theory. As the wave propagates, its magnitude decays gradually due to viscosity. As shown by Lamb,[68] the wave amplitude satisfies

$$a(t) = a_0 e^{-2\nu k^2 t}. \tag{25}$$

As shown in Fig. 6, the level-set simulations agree very well with the theoretical solution given by Eq. (25) over the 35 wave periods simulated, over which the wave amplitude decays to only 1% of its initial value. To show the convergence of the level-set simulation with respect to the grid resolution, three resolutions of 64×64, 128×128, and 256×256 are considered here. The

This article is copyrighted as indicated in the article. Reuse of AIP content is subject to the terms at: http://scitation.aip.org/termsconditions. Downloaded to IP: 129.7.106.213 On: Tue, 19 Jan 2016 17:21:50

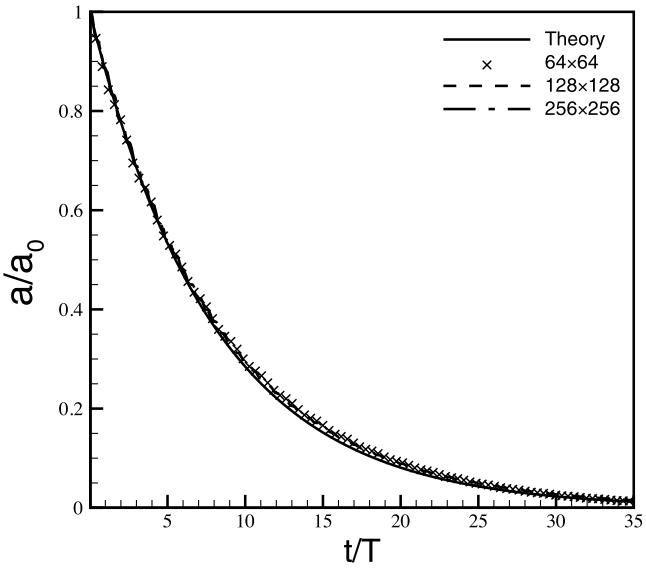

FIG. 6. Decay of the amplitude of a linear viscous wave from both theoretical prediction and the level-set simulations with various resolutions. Here, a_0 is the initial wave amplitude, and $T = 2\pi/\omega$ is the wave period.

simulated wave decay rates agree well with the analytical solution, with the agreement improving as the grid resolution increases.

C. Flow around a cube mounted on flat ground

Next, a turbulent boundary layer flow over a ground-mounted cube is simulated to test the near-field LES and the wall-layer-modeled immersed boundary method. A sketch of the problem is shown in Fig. 7. Simulation parameters are chosen to match those reported in Castro and Robins.[7] In particular, the size of the computational domain is $L_x \times L_y \times L_z = 18h \times 9h \times 5h$, where $h = 20$ cm is the edge length of the cube. In the x-, y-, and z-directions, 128, 128, and 64

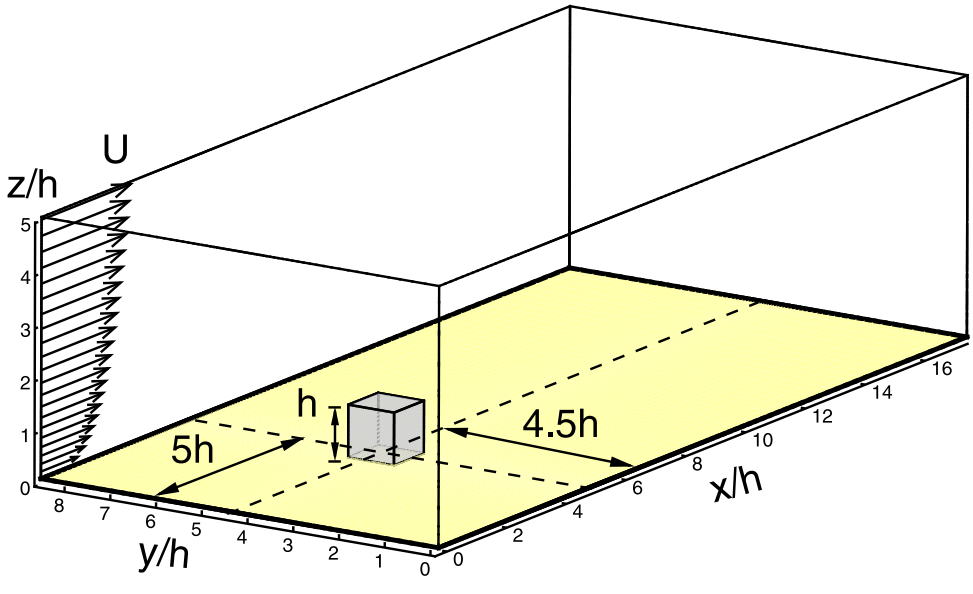

FIG. 7. Sketch of the simulation of a turbulent boundary layer flow around a cube mounted on flat ground.

This article is copyrighted as indicated in the article. Reuse of AIP content is subject to the terms at: http://scitation.aip.org/termsconditions. Downloaded to IP: 129.7.106.213 On: Tue, 19 Jan 2016 17:21:50

TABLE I. List of experimental and numerical datasets for validating the immersed boundary method module in the current near-field LES solver. Our LES test case is configured based on the parameters in Castro and Robins.[7]

Dataset	Data generation method	$Re_h = U_h h/\nu$
Baines [6,a]	Wind tunnel measurement	30 000
Vasilic-Melling[69,b]	RANS with κ-ϵ model	Not given
Castro and Robins[7]	Wind tunnel measurement	100 000
Paterson and Apelt[70]	RANS with κ-ϵ model	50 000–100 000
Murakami *et al.*[11]	RANS with κ-ϵ model	84 000
Richards *et al.*[8]	Field experiment	$O(10^6)$

[a]Data were reproduced from Fig. 2 in Richards *et al.*[8]
[b]Data were reproduced from Fig. 4 in Paterson and Apelt.[70]

grid points are used, respectively. This provides 13^3 grid points for resolving the cube. Following Castro and Robins,[7] the ground roughness length is set to be $z_0 = 0.02h$, the friction velocity is $u_* = 0.1U_h$, where U_h is the mean upstream wind speed at $z = h$, and the Reynolds number defined as $Re_h = U_h h/\nu$ is 1×10^5. The inflow condition is obtained from a precursor simulation of a fully developed turbulent boundary layer without the presence of the cube. A radiation condition is applied at the outflow boundary, and periodic condition is used on the spanwise boundaries. Wall-layer model is applied on the ground, and free-slip condition is applied on the top boundary.

To validate the immersed boundary method module in the current near-field LES solver, we compare our LES results with the experimental and numerical data in the literature. Table I lists the data collected for the validation. Figure 8 shows comparison of the mean streamwise velocity profiles between the present result and previous experimental and numerical data at three downstream locations on the central vertical plane. At all of the three locations, our results agree well with the literature, indicating that the present numerical tool is capable of capturing complex flow motions such as the flow separation and reattachment behind the object.

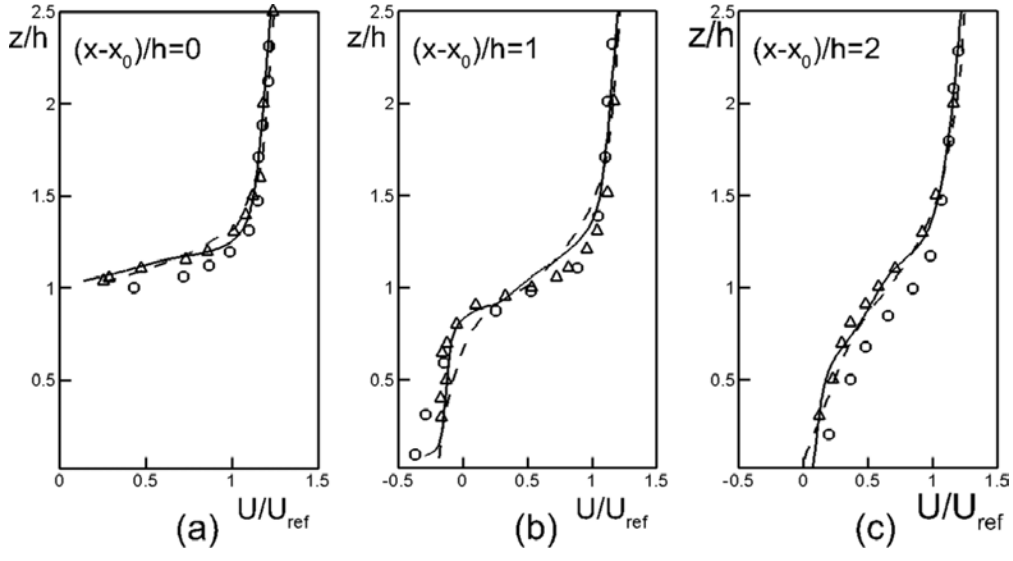

FIG. 8. Comparison of the profiles of mean streamwise velocity on the central vertical plane at downstream locations of (a) $(x - x_0)/h = 0$, (b) $(x - x_0)/h = 1.0$, and (c) $(x - x_0)/h = 2.0$, with x_0 being the streamwise coordinate at the center of the cube. U_{ref} is the mean velocity at the height of $z/h = 3$. The solid lines are the present results, open triangles are the data from Castro and Robins,[7] open circles are the data from Vasilic-Melling,[69] and the dashed lines are the results from Paterson and Apelt.[70]

This article is copyrighted as indicated in the article. Reuse of AIP content is subject to the terms at: http://scitation.aip.org/termsconditions. Downloaded to IP: 129.7.106.213 On: Tue, 19 Jan 2016 17:21:50

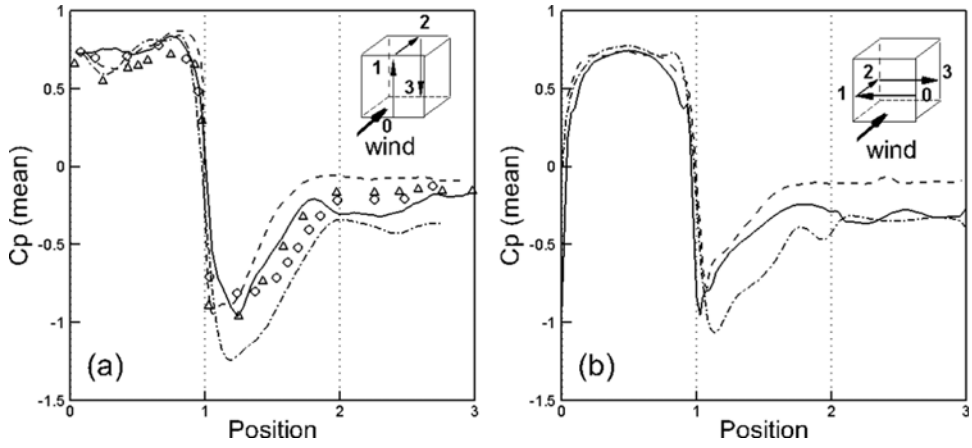

FIG. 9. Comparisons of distributions of pressure coefficient (a) along the vertical central line of the cube, and (b) along the horizontal central line of the cube. The solid lines are from the present simulation, dashed lines are from Castro and Robins,[7] dashed-dotted lines are from Richards *et al.*,[8] open triangles are from Murakami *et al.*,[11] and open circles are from Baines.[6]

The pressure coefficient distributions along the vertical and horizontal central lines on the cube are shown in Fig. 9. The pressure coefficient is defined as

$$Cp = \frac{p - p_r}{\frac{1}{2}\rho_a U_h^2}. \tag{26}$$

Here, p is the dynamic pressure, p_r is the reference pressure chosen at the upstream corner of the domain. As shown in the figure, the highest pressure occurs at the stagnation point on the frontal face, and the lowest pressure occurs on the leading edges of the roof and the side walls where the flow separates. Our results match well with previous experimental and numerical data, especially on the frontal face. The deviations among different cases are more discernible on the other faces where the flow separates.

IV. RESULTS

Having the numerical methods validated in Sec. III, the simulation results of flows past a semi-submersed rectangular prism in various wave fields are discussed here. Referring to Part 2 of Fig. 1, the near-field computational domain is 600 m long in the streamwise direction and has the dimensions of 300 m in both the spanwise and vertical directions. The total height of the object is $2h = 100$ m. Here, h is the height above and below the mean water level. The object has the aspect ratio of length : width : height = 1 : 1 : 2. A Cartesian mesh with a 192 (streamwise) × 128 (spanwise) × 128 (vertical) grid is used, with the grid points clustered near the object and the water surface. The center of the object is located at $(x_0, y_0, z_0) = (150\text{ m}, 150\text{ m}, 0\text{ m})$ in the computational domain, with the origin of the z-axis at the mean air–water interface. Periodic boundary condition is used on the spanwise boundaries, and both the water bottom and air top boundaries are treated as free-slip. The inflow condition is obtained from the precursor far-field simulation, and a radiation boundary condition is used at the outflow boundary to suppress numerical reflection. For the near-field simulation, the corresponding Reynolds number based on the object size is $Re_h = U_h h/\nu \approx 2.7 \times 10^7$, which falls in the fully turbulent regime. We remark that the height of the near-field domain is smaller than that of the precursor far-field simulation. The extraction of inflow condition from a larger domain can cause small spurious pile-up of turbulent kinetic energy at the top boundary near the inlet in the near-field simulation. This extra energy gets dissipated and advected out of the domain with the outflow. The vertical distance from the top boundary of the computational domain to the object roof is chosen to be sufficiently large so that this small pile-up of energy does not impact the near-object flow investigated in this study.

This article is copyrighted as indicated in the article. Reuse of AIP content is subject to the terms at: http://scitation.aip.org/termsconditions. Downloaded to IP: 129.7.106.213 On: Tue, 19 Jan 2016 17:21:50

Three wind-wave conditions are considered. First, JONSWAP waves as in Sec. III A are studied (referred as Case-JON hereby). Then, superimposed to the local JONSWAP waves, two swell cases with steepnesses of $ak = 0.1$ and $ak = 0.15$ are considered (referred to as Case-SW010 and Case-SW015). The swells have a wavelength of 200 m, and the phase speed can be estimated as 17.7 m/s according to the linear wave dispersion relation. Both the swells and the dominant JONSWAP waves propagate in the x-direction, normal to the frontal face of the object. The mean wind speed at the height of 10 m above the sea surface, U_{10}, is 9.5 m/s. For wind–wave interactions, the wave age, defined as the ratio of wave phase speed to the characteristic wind velocity, is an important parameter to quantify the relative propagation speed of wave to wind.[15] Here, the wave ages are, respectively,

$$\frac{C_{peak}}{U_{10}} = 1.05, \quad \frac{C_{swell}}{U_{10}} = 1.86, \tag{27}$$

where C_{peak} is the phase speed of the waves at the JONSWAP spectrum peak, and C_{swell} is the phase speed of the swells. Normalized wave spectral density, which is obtained by performing Fourier transform of the incoming wave surface elevations in the x-direction then averaging in the y-direction, is plotted as a function of the normalized wavenumber in Fig. 10. As shown, the spectra are similar in the three cases. In the presence of swells, the large peak at the wavenumber corresponding to the swells is noteworthy.

The wind load force D_{wind} acting on the object is calculated as the difference of air pressure forces on the frontal and rear faces of the object, i.e., the form drag on this bluff object. The viscous force is negligibly small compared with the form drag, with a difference of two orders of magnitude. The wind load coefficient is defined as

$$Cd_{wind} = \frac{D_{wind}}{\frac{1}{2}\rho_a U_r^2 A}, \tag{28}$$

where U_r is the reference velocity, which is defined as the upstream wind speed averaged in time at the point $(x_0 - 2h, y_0, z_0 + h)$, and A is the area of the windward side of the object above the instantaneous water surface. We remark that by allowing A to vary with the wave surface elevation, the variation in Cd_{wind} represents the effect of the wave-induced pressure variation on the windward, above-surface face of the stationary object. The temporal variations of Cd_{wind} and the normalized incident wave elevation $\langle \eta_i \rangle$ for the three cases are shown in Fig. 11, where the abscissa axis is the normalized relative time $t - t_0$ and t_0 is chosen subjectively after the flow is fully developed. Note that the swell period $T_{swell} \approx 11.3$ s is used for a consistent normalization in all cases, including

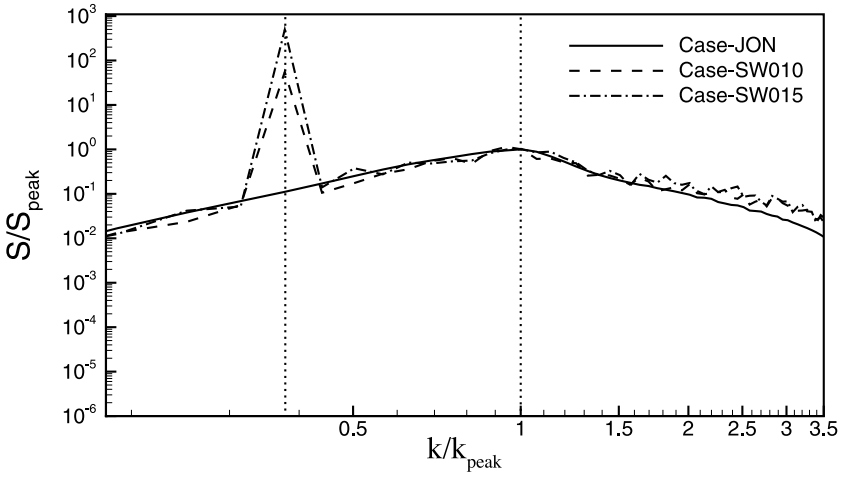

FIG. 10. Normalized energy spectral density of the incoming waves of the three cases. Here, S is the wave spectral density, k is the wavenumber, and the subscript "peak" denotes the peak of the JONSWAP waves. Dotted lines represent the normalized wavenumber of the swells (left) and the normalized peak wavenumber of the JONSWAP waves (right).

This article is copyrighted as indicated in the article. Reuse of AIP content is subject to the terms at: http://scitation.aip.org/termsconditions. Downloaded to IP: 129.7.106.213 On: Tue, 19 Jan 2016 17:21:50

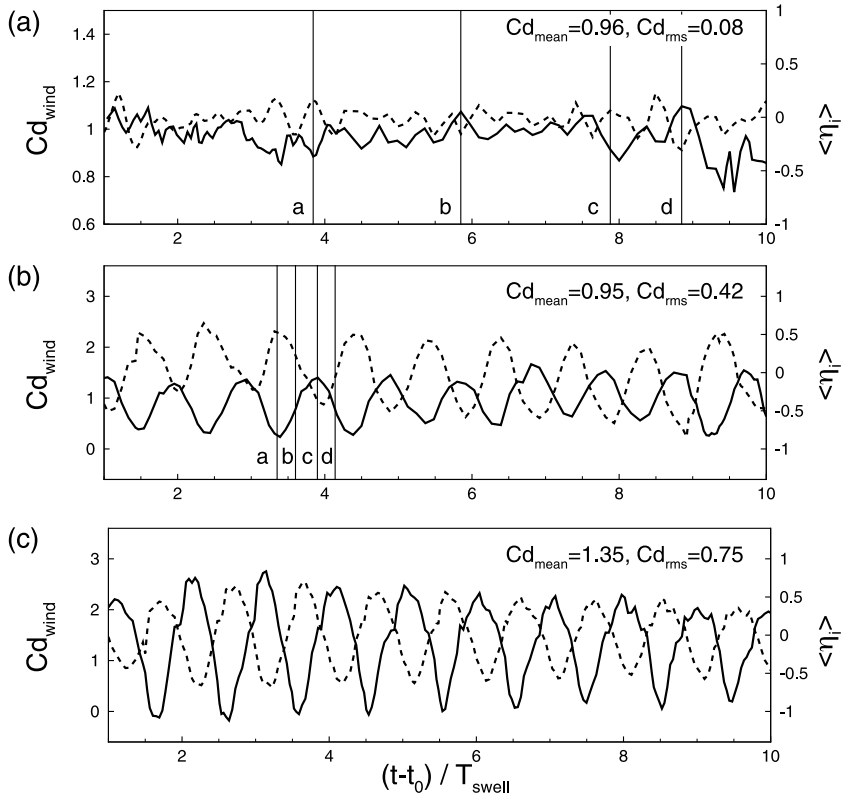

FIG. 11. Temporal variations of the wind load coefficient, Cd_{wind} (solid line), and the averaged wave surface elevation at the frontal face of the object, $\langle \eta_i \rangle$ (dashed line), for (a) Case-JON, (b) Case-SW010, and (c) Case-SW015. The abscissa axis is the time normalized by the period of the swells. The thin vertical lines in (a) and (b) denote the instants shown in Figs. 14 and 18.

Case-JON in which there is no swell, simply for the purpose of comparison. Here, $\langle \eta_i \rangle$ is defined as the spanwisely averaged (over the width of the object, where the spacial variation is less significant compared with that over the whole domain width) wave surface elevation arriving at the frontal face of the object, and is normalized by the significant wave height of the JONSWAP waves in Case-JON and by the swell wave heights in Case-SW010 and Case-SW015.

Figure 11 shows that Cd_{wind} oscillates in time for all three cases. Particularly, there exists a clear correlation between the wind load and the waves as shown in Figs. 11(b) and 11(c) where swells dominate. A phase shift close to 180° between Cd_{wind} and $\langle \eta_i \rangle$ is observed. For Case-JON shown in Fig. 11(a), the dependence of the wind load on the wave is less obvious due to the lack of a significant wave component. It is also found that the mean wind load coefficient and the amplitude of oscillation are dependent on the wave conditions. In Case-JON, the mean wind load coefficient Cd_{mean} is about 0.96 and the oscillation is relatively small and irregular. In Case-SW010, where a swell is present, the oscillation is much larger compared with that in Case-JON, i.e., the root-mean-square value of the wind load coefficient Cd_{rms} is about 0.42 compared to $Cd_{rms} \approx 0.08$ in Case-JON, while its mean load coefficient is almost the same as that in the Case-JON. When a larger swell is present in Case-SW015, both the amplitude of the oscillations and the mean wind load coefficient are significantly increased, with $Cd_{mean} \approx 1.35$ and $Cd_{rms} \approx 0.75$. The larger oscillation is expected, and the increased mean wind load is also not surprising considering that some kinetic energy is transferred from the swell to the wind so that the wind speed near the water surface is augmented.[4,21]

The correlations between instantaneous Cd_{wind} and $\langle \eta_i \rangle$ are shown in Fig. 12. In Case-JON, the data are scattered without a clear pattern around $Cd_{wind} = 1$ and $\langle \eta_i \rangle = 0$. With the presence of swells [Figs. 12(b) and 12(c)], the data are almost linearly correlated with a negative slope. The

This article is copyrighted as indicated in the article. Reuse of AIP content is subject to the terms at: http://scitation.aip.org/termsconditions. Downloaded to IP: 129.7.106.213 On: Tue, 19 Jan 2016 17:21:50

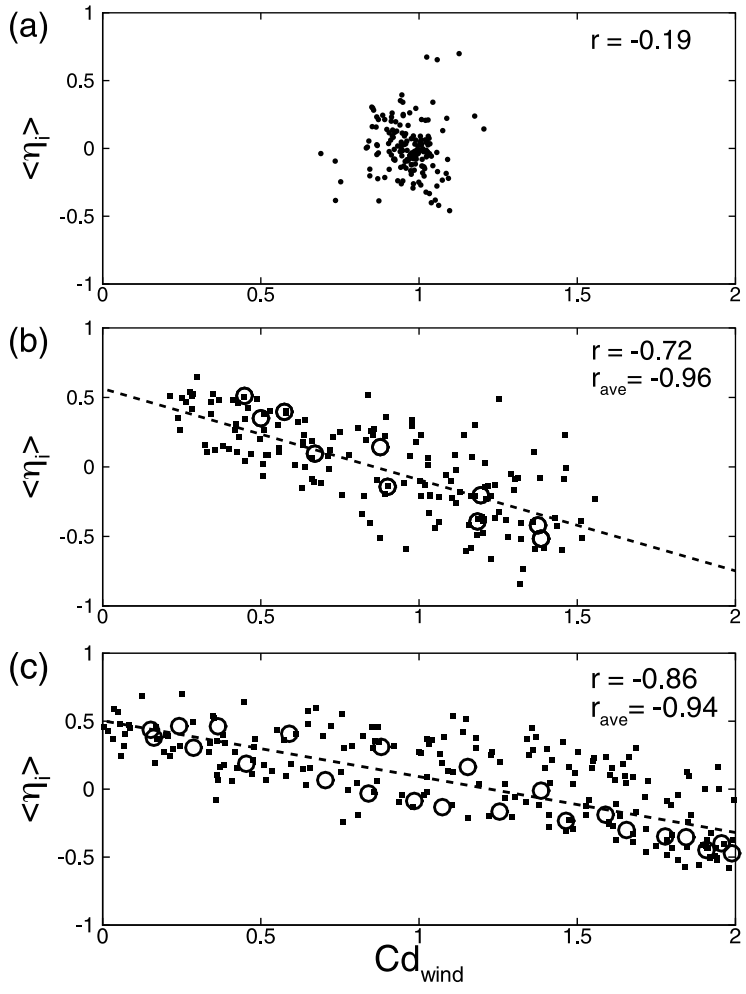

FIG. 12. Correlation between wind load coefficient Cd_{wind} and averaged wave surface elevation at the frontal face of the object $\langle \eta_i \rangle$, for (a) Case-JON, (b) Case-SW010, and (c) Case-SW015. Scattered solid dots are instantaneous data, the open circles in (b) and (c) are phase-averaged results, and the dashed lines in (b) and (c) are least-square regression lines of the instantaneous data. Correlation coefficient r is defined in Eq. (29).

slope of the least-square regression line is flatter in Case-SW015 (about −0.41) than in Case-SW010 (about −0.65), due to increased wind drag variation. Figure 13 plots the averaged values of Cd_{wind} and $\langle \eta_i \rangle$ with respect to the swell phases (known as the phase averaging). It shows that the variation amplitude of the phase-averaged Cd_{wind} is approximately 48% larger in Case-SW015 than in Case-SW010. Quantitatively, the correlation coefficient is calculated as follows:

$$r = \frac{\sum_{n=1}^{N} \left[\left(Cd_{wind,n} - \overline{Cd}_{wind} \right) \left(\langle \eta_i \rangle_n - \overline{\langle \eta_i \rangle} \right) \right]}{\sqrt{\sum_{n=1}^{N} \left(Cd_{wind,n} - \overline{Cd}_{wind} \right)^2} \sqrt{\sum_{n=1}^{N} \left(\langle \eta_i \rangle_n - \overline{\langle \eta_i \rangle} \right)^2}}, \tag{29}$$

where N is the number of samples and the overline denotes the ensemble mean value. The values obtained are as follows: $r \approx -0.19$ for Case-JON, $r \approx -0.72$ for Case-SW010, and $r \approx -0.86$ for Case-SW015. After the phase averaging, r_{ave} is increased to −0.96 for Case-SW010 and −0.94 for Case-SW015 [Figs. 12(b) and 12(c)].

Although the correlation between Cd_{wind} and $\langle \eta_i \rangle$ is much weaker in Case-JON, the instantaneous flow fields plotted in Fig. 14 indicate that appreciable pressure variations on the frontal face of the object can be caused by the JONSWAP waves, i.e., when a wave crest arrives at the object [Figs. 14(a) and 14(c)], the pressure on the frontal face is lower compared with the cases

This article is copyrighted as indicated in the article. Reuse of AIP content is subject to the terms at: http://scitation.aip.org/termsconditions. Downloaded to IP: 129.7.106.213 On: Tue, 19 Jan 2016 17:21:50

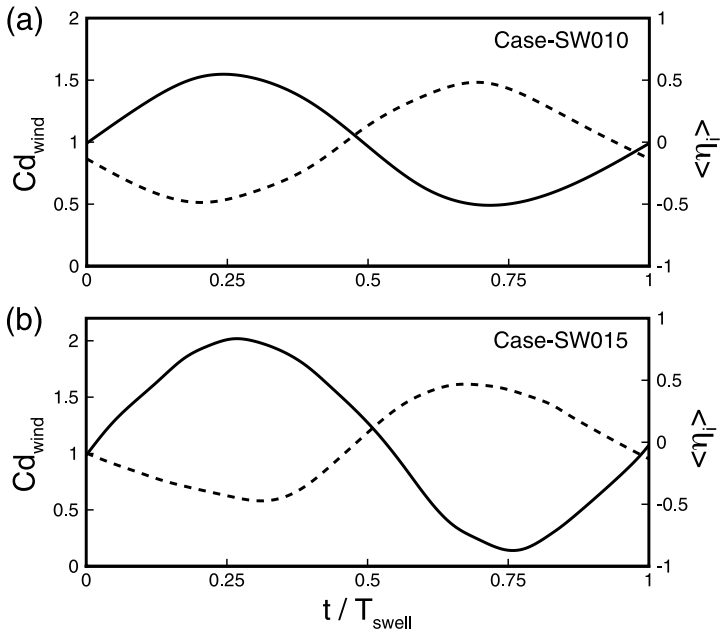

FIG. 13. Phase-averaged wind load coefficient Cd_{wind} (solid line) and averaged wave surface elevation at the frontal face of the object $\langle \eta_i \rangle$ (dashed line), for (a) Case-SW010 and (b) Case-SW015. T_{swell} is the wave period of the swells.

when a trough arrives [Figs. 14(b) and 14(d)]. Furthermore, in Fig. 15 where the spectra of wind load and wave surface elevation are obtained by performing Fast Fourier Transform (FFT) over the temporal data, the peak of the wind load spectrum occurs at almost the same location as the peak frequency of the JONSWAP waves. Note that the good match between the simulated wave

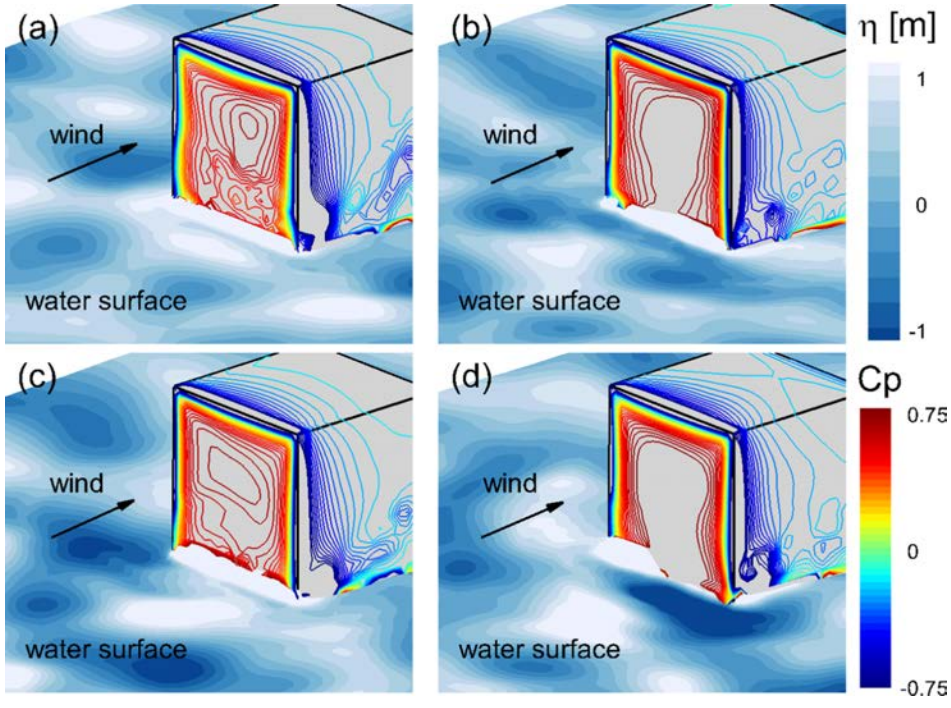

FIG. 14. Four instantaneous flow fields around the object for Case-JON. The color contours denote wind pressure coefficient Cp on the surfaces of the object, and the blue-scale contours denote the elevation η of the wave surface. The time instants are shown in Fig. 11(a).

This article is copyrighted as indicated in the article. Reuse of AIP content is subject to the terms at: http://scitation.aip.org/termsconditions. Downloaded to IP: 129.7.106.213 On: Tue, 19 Jan 2016 17:21:50

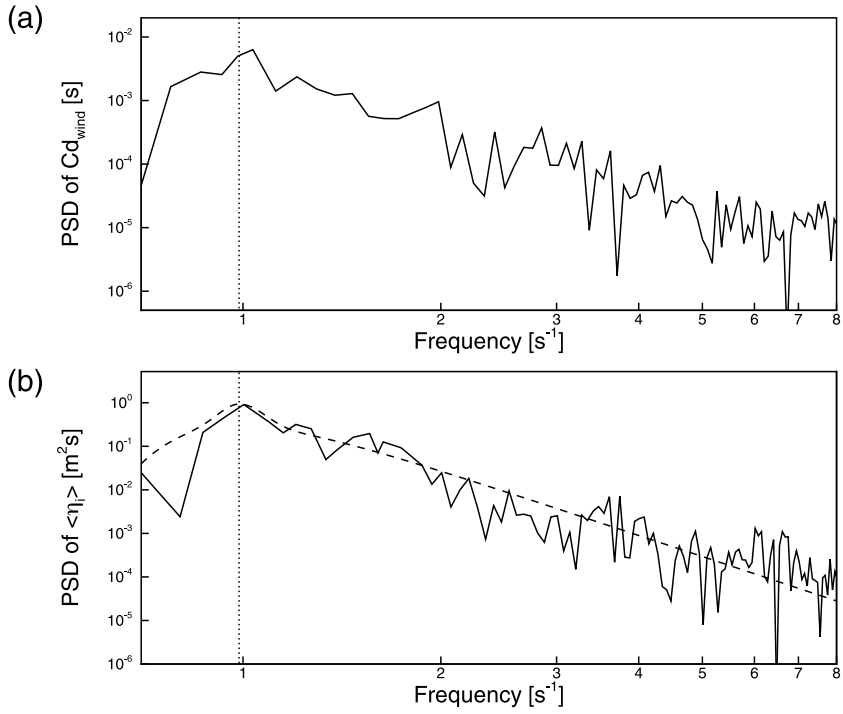

FIG. 15. Power spectral densities (PSDs) of (a) wind load coefficient Cd_{wind} and (b) spanwisely averaged wave surface elevation at the frontal face of the object $\langle \eta_i \rangle$ for Case-JON. The dashed line in (b) represents the theoretical JONSWAP wave spectrum, and the dotted line indicates its peak wavenumber ($\approx 0.986\ s^{-1}$).

spectrum and its theoretical form shows a good validation of the current code, despite the oscillations observed in the temporal FFT spectrum. As discussed by Sullivan *et al.*[16] and Yang and Shen[19] the wave effects on winds can reach up to a height of approximately one wavelength above the water surface. Considering that the peak wavelength of the JONSWAP waves here is 63.3 m, which is comparable to the height of the object above the water (i.e., 50 m), it is not surprising that the wind load is influenced by the waves. Also as expected, this effect deceases moving away from the wave surface. The reason that no clear correlation is shown in Fig. 11(a) is because that there are many wave components influencing the air motion simultaneously, unlike Case-SW010 and Case-SW015 where swells dominate.

With their long wavelengths and large wave heights, the swells induce significant effects on air pressure distribution on the object's frontal face. Figure 16 shows the distribution of phase-averaged wind pressure coefficient on the five faces of the object in Case-SW010. The pressure coefficient is higher when swell troughs arrive at the frontal face than when swell crests arrive. At the crest phase, the pressure maximum occurs at the upper part of the frontal surface, while at the trough phase the pressure is higher at the lower part near the water surface. On the rear face of the object, the variation of wind pressure with different swell phases is relatively small but still noticeable.

Next, the mechanisms of the dependence of wind load on waves are discussed using Case-SW010 as an example. First, the air flow above the waves without the presence of the object is examined. Note that the wind speed is $U_{10} = 9.5$ m/s here, while the swell phase velocity is 17.7 m/s. Under such a strong swell condition, a forward thrust on the wind exists above the swell trough, i.e., the swell pushes the wind to move faster there.[21] Consequently, even without the object, a velocity variation pattern is formed, as shown in Fig. 17 in which the spanwise-averaged streamwise velocity $\langle u \rangle / U_{ref}$ from the precursor simulation is plotted. It is observed that the wind speed has its maximum approximately above swell trough and its minimum approximately above swell crest, consistent with previous studies.[5,17,21] This spatial variation of wind speed is particularly strong in the near-surface region where the object is placed. Therefore, high (low) pressure on the object's frontal face is induced by the high (low) wind speed above the trough (crest).

This article is copyrighted as indicated in the article. Reuse of AIP content is subject to the terms at: http://scitation.aip.org/termsconditions. Downloaded to IP: 129.7.106.213 On: Tue, 19 Jan 2016 17:21:50

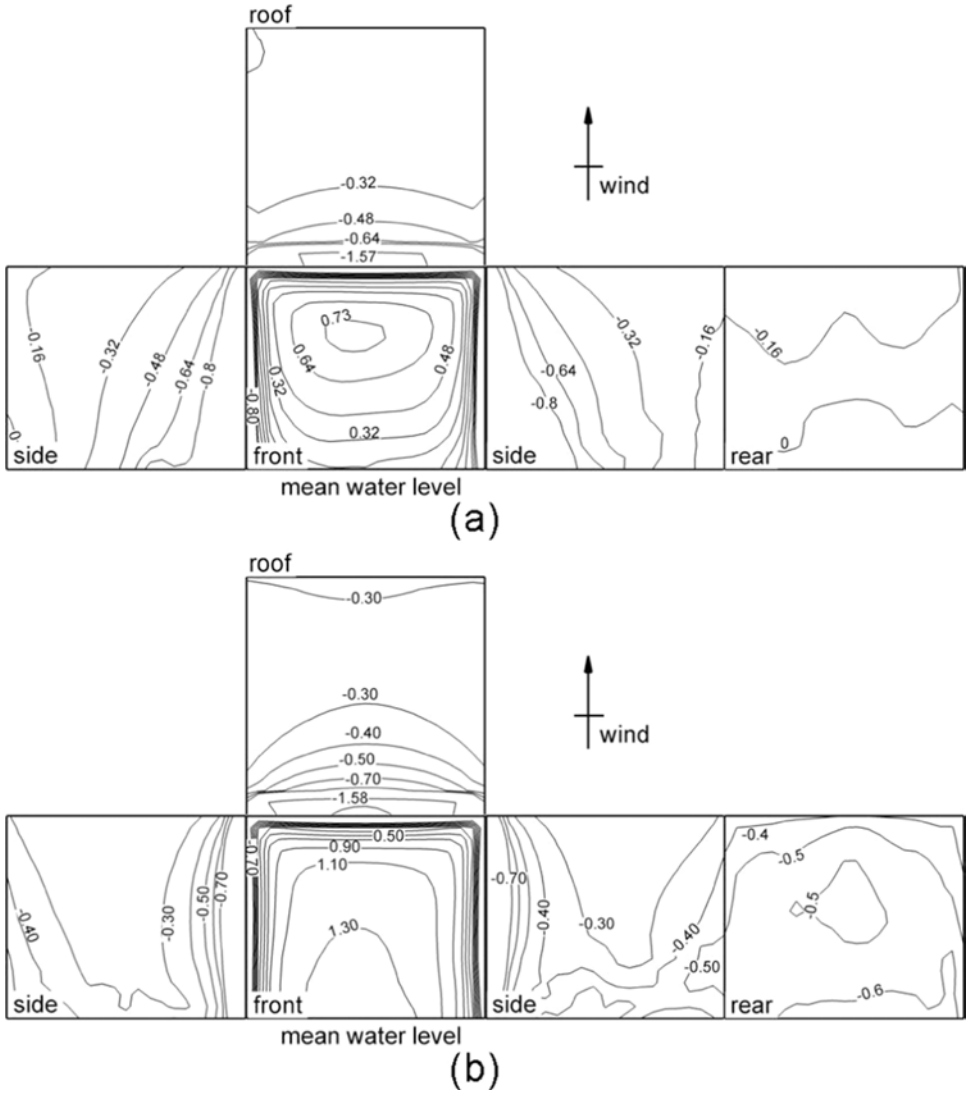

FIG. 16. Contours of wind pressure coefficient Cp on the surfaces of the object averaged over the (a) crests and (b) troughs of the swells in Case-SW010.

In addition, the presence of the object induces a blockage effect, which makes the wave-induced air pressure fluctuations on the frontal face of the object even larger. This can be seen from the instantaneous flow field. As shown in Fig. 18(a), when a swell crest approaches the frontal face, there exits a wide region of low wind speed near the lower part of the object. The wind tends to move vertically due to the vertical motion of the wave surface as well as the blockage of the object, thus only a small portion of the wind near the object is normal to the frontal face, resulting in a relatively lower pressure. In Fig. 18(b), after the swell crest passes the object, a large portion of the velocity vectors near the object turn downwards following the drop of the water surface. As a compensation, the wind speed at the upper part of the object increases, leading to an increase in surface pressure. In Fig. 18(c), when a swell trough arrives, the downward flow reaches its lowest point and most of the wind vectors are aligned normal to the frontal surface of the object, and the low wind speed region in front of the object is minimized. As a result, the pressure on the frontal face reaches its maximum. Additionally, a small jet with higher streamwise velocity is formed close to the water surface, which also contributes to the high surface pressure on the lower part of the object. In Fig. 18(d), when the water surface goes up again, the velocity vectors near the water surface show strong upward motions, the jet diminishes, and the pressure drops.

This article is copyrighted as indicated in the article. Reuse of AIP content is subject to the terms at: http://scitation.aip.org/termsconditions. Downloaded to IP: 129.7.106.213 On: Tue, 19 Jan 2016 17:21:50

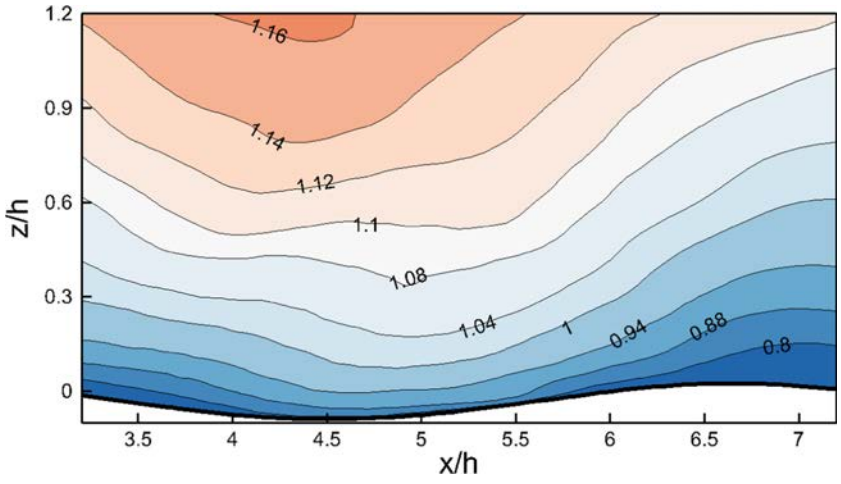

FIG. 17. Normalized streamwise wind velocity u/U_{10} in the swell-phase-averaged local wind field for Case-SW010 without the presence of the object.

The wave-induced variations can be visualized in averaged wind fields around the object, as shown in Fig. 19. The pressure coefficient varies significantly under different wave conditions. As discussed earlier, the pressure in front of the object is high when a swell trough arrives and low when a swell crest arrives. A vortex at the front corner of the object is observed in all the three cases, which moves with wave motions. Especially, in presence of swells (Case-SW010 and Case-SW015), the vortex moves upper backwards above the swell crest. On the other hand, when the trough arrives, the vortex moves downwards with the water surface, and the vortex-induced flow is weaker in front of the object.

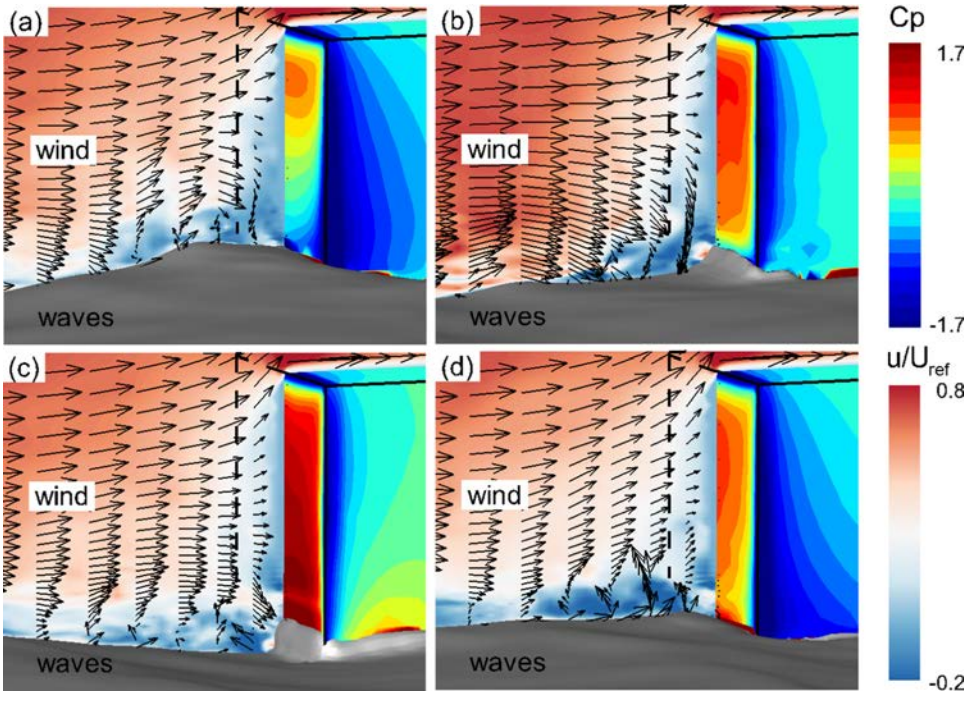

FIG. 18. Four instantaneous wind fields around the object at different phases of the incoming swell in Case-SW010. The normalized streamwise wind velocity u/U_{10} is plotted on the central vertical plane together with velocity vectors on it, and the pressure coefficient Cp is plotted on the surfaces of the object. The vectors are plotted for every 4 and 2 points in the streamwise and vertical directions, respectively. The time instants are shown in Fig. 11(b).

This article is copyrighted as indicated in the article. Reuse of AIP content is subject to the terms at: http://scitation.aip.org/termsconditions. Downloaded to IP: 129.7.106.213 On: Tue, 19 Jan 2016 17:21:50

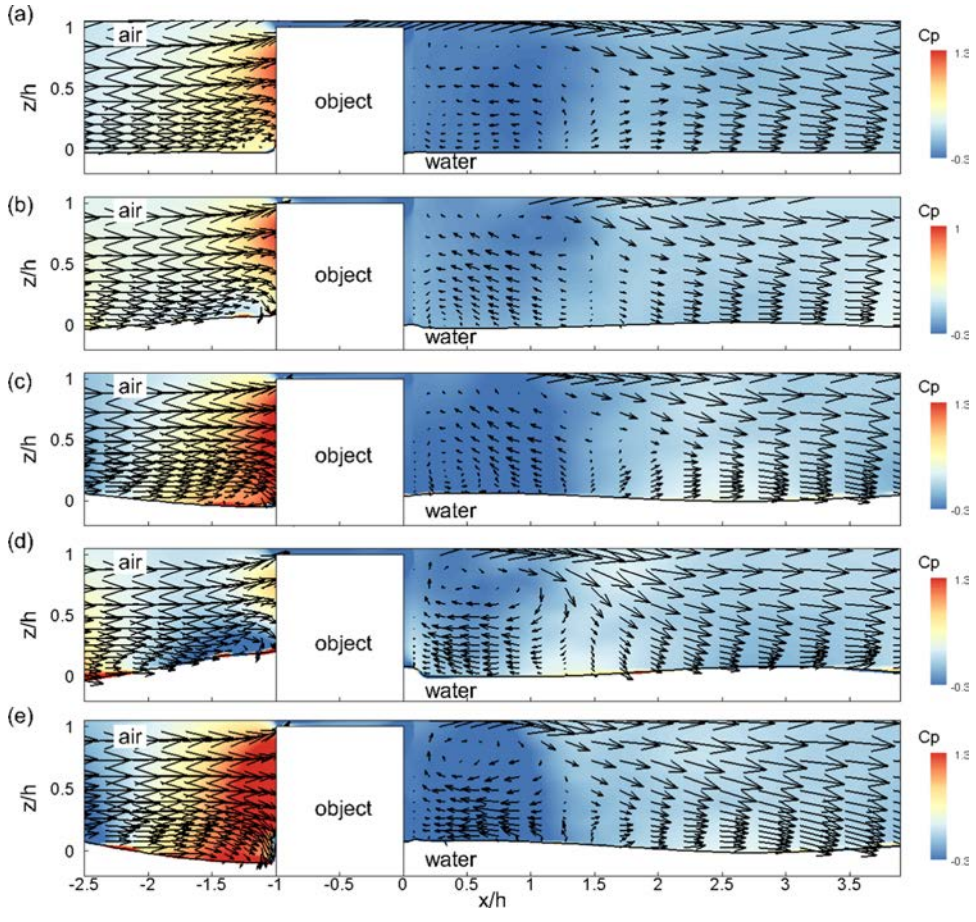

FIG. 19. Wind fields around the object on the vertical central plane: (a) time averaged for Case-JON, (b) phase-averaged with respect to the wave crests arriving at frontal face of the object for Case-SW010, (c) phase-averaged with respect to the wave troughs arriving at frontal face of the object for Case-SW010, (d) phase-averaged with respect to the wave crests arriving at frontal face of the object for Case-SW015, and (e) phase-averaged with respect to the wave troughs arriving at frontal face of the object for Case-SW015. The contours of C_p are shown on the vertical plane. For clarity in visualization, the velocity vectors are plotted for every four grid points in both the x and z-directions. Only a small portion of the computational domain is plotted.

The flow patterns behind the object are also shown in Fig. 19. Although the wave-induced pressure variation is also observed on the leeward side of the object, its contribution to the wave-induced variation of the wind load is not significant because we found that it is at least one order of magnitude smaller than the wave-induced pressure variation on the windward face. Although the wave motions behind the object are much weaker compared to those in the front, their effects on the wakes in the air part are still discernible. In the wakes behind the object, similar to the flow past a blunt object mounted on a flat surface (Sec. III C), a recirculation region with lower pressure due to flow separation is observed. The pressure in the recirculation region is further reduced when the water surface is relatively high. Moreover, the length of the separation bubble appears to be dependent on the wave conditions. It decreases with the swell height (compare Case-SW010 and Case-SW015), but with stronger reversed flow inside. In other words, the reattachment happens earlier when the swell amplitude increases. Furthermore, the vortex center in the recirculation region moves with the swell. In Case-SW010, the vortex center is located at $x/h \approx 1.09$ when the crest arrives at the frontal face [Fig. 19(b)], and is at $x/h \approx 0.90$ when the trough arrives [Fig. 19(c)], whereas in Case-SW015, it occurs at $x/h \approx 0.39$ when the crest arrives [Fig. 19(d)], and at $x/h \approx 0.44$ when the trough arrives [Fig. 19(e)].

This article is copyrighted as indicated in the article. Reuse of AIP content is subject to the terms at: http://scitation.aip.org/termsconditions. Downloaded to IP: 129.7.106.213 On: Tue, 19 Jan 2016 17:21:50

V. CONCLUSIONS

In this paper, the wind loads on a semi-submersed rectangular prism in various oceanic wave fields have been studied using large-eddy simulations. In the far field upstream, wind and wave fields are simulated as precursors with a dynamically coupled wind LES and wave HOSM simulation approach. This far-field simulation provides physical wind and wave inflow conditions for studying the flow structure around a semi-submersed object. In the near field surrounding the object, a level-set method is used for the local wind–wave interaction and an immersed-boundary method is used for modeling the semi-submersed object. With these numerical tools, the wind pressure on the surfaces of the object and the flow patterns around the object have been studied with different wave conditions.

In this study, both broadband wind-generated waves (satisfying the JONSWAP spectrum) and long-crest ocean swells are considered. The results show that the wave field has an appreciable effect on the wind load of the semi-submersed object. The wind drag is found to oscillate with the incident waves. In the case with JONSWAP waves only, where the wave surface is complex and lack of a dominant wave component, the correlation is less obvious in the instantaneous data, but can be revealed clearly in the spectral space. When the wave field has a dominant swell component, the correlation is clear and strong. There exists a nearly 180° of phase difference between the wind drag and the incident swell, meaning that the wind drag is larger when a swell trough arrives and is smaller when a crest arrives. The variations in the wind load are primarily due to the wind distortion caused by the fast-traveling swells, namely, the faster (resp. slower) wind speed above the swell trough (resp. crest). Furthermore, the blockage of the object changes the local flow patterns according to various wave phases, which further enhances the wind load variations.

The air flow patterns around the object vary with the underlying wave motions. In front of the object, the position, and strength of the corner vortex vary periodically with the incident swells. Behind the object, although the waves are smaller, both the length and strength of the wake recirculation region are still wave-phase dependent. Thus, the pressure on the back of the object also oscillates with wave conditions, with smaller magnitudes compared to the oscillations on the frontal face.

Finally, we remark that this study serves as a first step in the research of wind loads in realistic ocean wave environment. The results show that waves can cause significant variations in wind loads. Such effects were not adequately recognized and have not been quantified in previous studies. Our results indicate that for improved modeling of wind loads, one should take into account the influences of different wave conditions and the temporal oscillations in the wind loads in addition to the mean loads. It should be noted that only several canonical cases were investigated in this study. At the next step, more complex wind and waves conditions, such as swells with various oblique angles to the local wind direction,[71–73] non-equilibrium wind–wave scenarios, breaking waves, as well as the responsive motions of the object, need to be considered. These subjects are beyond the scope of the current study but should be investigated in future research.

ACKNOWLEDGMENTS

The support to L.S. through NSF No. CBET-1341062 and ONR No. N00244-14-2-0008 is gratefully acknowledged. D.Y. acknowledges the support from start-up funds at University of Houston.

[1] J. Wills, "Recent research on wind loading," Philos. Trans. R. Soc., A **334**, 229 (1991).
[2] W. Blendermann, "Ships may encounter high wind loads—A statistical assessment," Proc. Mech. E Part M J. Eng. Marit. Environ. **218**, 1 (2004).
[3] N. Haritos, "Introduction to the analysis and design of offshore structures—An overview," Electron. J. Struct. Eng. **7**, 55 (2007).
[4] D. Yang, C. Meneveau, and L. Shen, "Large-eddy simulation of offshore wind farm," Phys. Fluids **26**, 025101 (2014).
[5] D. Yang, C. Meneveau, and L. Shen, "Effect of downwind swells on offshore wind energy harvesting–A large-eddy simulation study," Renewable Energy **70**, 11 (2014).
[6] W. Baines, "Effects of velocity distribution on wind loads and flow patterns on buildings," in *Proceedings of the Symposium on Wind Effects on Buildings and Structures* (National Physical Laboratory, Teddington, England, 1963).

This article is copyrighted as indicated in the article. Reuse of AIP content is subject to the terms at: http://scitation.aip.org/termsconditions. Downloaded to IP: 129.7.106.213 On: Tue, 19 Jan 2016 17:21:50

[7] I. Castro and A. Robins, "The flow around a surface-mounted cube in uniform and turbulent streams," J. Fluid Mech. **79**, 307 (1977).
[8] P. Richards, R. Hoxey, and L. Short, "Wind pressure on a 6 m cube," J. Wind Eng. Ind. Aerodyn. **89**, 1553 (2001).
[9] J. Hunt, C. Abell, J. Peterka, and H. Woo, "Kinematical studies of flows around free or surface-mounted obstacles; applying topology to flow visualization," J. Fluid Mech. **86**, 179 (1978).
[10] S. Murakami, A. Mochida, and K. Hibi, "Three-dimensional numerical simulation of air flow around a cubic model by means of large eddy simulation," J. Wind Eng. Ind. Aerodyn. **25**, 291 (1987).
[11] S. Murakami, A. Mochida, Y. Hayashi, and S. Sakamoto, "Numerical study on velocity-pressure filed and wind forces for bluff bodies by κ-ϵ, ASM and LES," J. Wind Eng. Ind. Aerodyn. **44**, 2841 (1992).
[12] R. Isherwood, "Wind resistance of merchant ships," Trans. Roy. Inst. Naval Architects **115**, 327 (1973).
[13] W. Blendermann, "Parameter identification of wind loads on ships," J. Wind Eng. Ind. Aerodyn. **51**, 339 (1994).
[14] O. Shemdin and E. Hsu, "Direct measurement of aerodynamic pressure above a simple progressive gravity wave," J. Fluid Mech. **30**, 403 (1967).
[15] S. Belcher and J. Hunt, "Turbulent flow over hills and waves," Annu. Rev. Fluid Mech. **30**, 507 (1998).
[16] P. P. Sullivan, J. McWilliams, and C. Moeng, "Simulation of turbulent flow over idealized water waves," J. Fluid Mech. **404**, 47 (2000).
[17] L. Shen, X. Zhang, D. Yue, and M. Triantafyllou, "Turbulent flow over a flexible wall undergoing a streamwise travelling wave motion," J. Fluid Mech. **484**, 197 (2003).
[18] N. Kihara, H. Hanazaki, T. Mizuya, and H. Ueda, "Relationship between airflow at the critical height and momentum transfer to the traveling waves," Phys. Fluids **19**, 015102 (2007).
[19] D. Yang and L. Shen, "Direct-simulation-based study of turbulent flow over various waving boundaries," J. Fluid Mech. **650**, 131 (2010).
[20] J. Jiménez, "Turbulent flows over rough walls," Annu. Rev. Fluid Mech. **36**, 173 (2004).
[21] P. P. Sullivan, J. Edson, T. Hristov, and J. McWilliams, "Large eddy simulations and observations of atmospheric marine boundary layers above non-equilibrium surface waves," J. Atmos. Sci. **65**, 1225 (2008).
[22] D. Yang and L. Shen, "Simulation of viscous flows with undulatory boundaries. II. Coupling with other solvers for two-fluid computations," J. Comput. Phys. **230**, 5510 (2011).
[23] D. Yang, C. Meneveau, and L. Shen, "Dynamic modelling of sea-surface roughness for large-eddy simulation of wind over ocean wave field," J. Fluid Mech. **726**, 62 (2013).
[24] A. Lang and M. Gharib, "Experimental study of the wake behind a surface-piercing cylinder for a clean and contaminated free surface," J. Fluid Mech. **402**, 109 (2000).
[25] P. Vlachos and D. Telionis, "The effect of free surface on the vortex shedding from inclined circular cylinders," J. Fluids Eng. **130**, 021103 (2008).
[26] H. Akilli and D. Rockwell, "Vortex formation from a cylinder in shallow water," Phys. Fluids **14**, 2957 (2002).
[27] T. Kawamura, S. Mayer, A. Garapon, and L. Sørensen, "Large eddy simulation of a flow past a free surface piercing circular cylinder," J. Fluids Eng. **124**, 91 (2002).
[28] G. Yu, E. Avital, and J. Williams, "Large eddy simulation of flow past free surface piercing circular cylinders," J. Fluids Eng. **130**, 101304 (2008).
[29] J. Suh, J. Yang, and F. Stern, "The effect of air-water interface on the vortex shedding from a vertical circular cylinder," J. Fluids Struct. **27**, 1 (2011).
[30] E. N. Wayman, P. D. Sclavounos, S. Butterfield, J. Jonkman, and W. Musial, "Coupled dynamic modeling of floating wind turbine systems," Report No. NREL/CP-500-39481, 2006, http://www.nrel.gov/docs/fy06osti/39481.pdf.
[31] D. Roddier, C. Cermelli, A. Aubault, and A. Weinstein, "WindFloat: A floating foundation for offshore wind turbines," J. Renewable Sustainable Energy **2**, 033104 (2010).
[32] R. J. A. M. Stevens, J. Graham, and C. Meneveau, "A concurrent precursor inflow method for large eddy simulations and applications to finite length wind farms," Renewable Energy **68**, 46 (2014).
[33] S. Osher and J. Sethian, "Fronts propagating with curvature-dependent speed: Algorithms based on Hamilton-Jacobi formulations," J. Comput. Phys. **79**, 12 (1988).
[34] M. Sussman, E. Fatemi, P. Smereka, and S. Osher, "An improved level set method for incompressible two-phase flows," Comput. Fluids **27**, 663 (1998).
[35] J. Sethian and P. Smereka, "Level set methods for fluid interfaces," Annu. Rev. Fluid Mech. **35**, 341 (2003).
[36] E. Fadlun, R. Verzicco, P. Orlandi, and J. Mohd-Yusof, "Combined immersed-boundary finite difference methods for three-dimensional complex flow simulations," J. Comput. Phys. **161**, 35 (2000).
[37] C. Peskin, "The immersed boundary method," Acta Numer. **11**, 479 (2001).
[38] R. Mittal and G. Iaccarino, "Immersed boundary methods," Annu. Rev. Fluid Mech. **37**, 2379 (2005).
[39] K. Hasselmann, T. Barnett, E. Bouws, H. Carlson, D. Cartwright, K. Enke, J. Ewing, H. Gienapp, D. Hasselmann, P. Kruseman, A. Meerburg, P. Müller, D. Olbers, K. Richter, W. Sell, and H. Walden, "Measurements of wind-wave growth and swell decay during the Joint North Sea Wave Project (JONSWAP)," Ergänzung zur Deut. Hydrogr. Z. **12**(A8), 1 (1973).
[40] A. Smedman, U. Hogstrom, H. Bergstrom, and A. Rutgersson, "A case study of airsea interaction during swell conditions," J. Geophys. Res. **104**, 25833, doi:10.1029/1999JC900213 (1999).
[41] V. Makin, "On the possible impact of a following-swell on the atmospheric boundary layer," Boundary Layer Meteorol. **129**, 469 (2008).
[42] D. Yang and L. Shen, "Simulation of viscous flows with undulatory boundaries. I. Basic solver," J. Comput. Phys. **230**, 5488 (2011).
[43] F. Porté-Agel, C. Meneveau, and M. Parlange, "A scale-dependent dynamic model for large-eddy simulation: Application to a neutral atmospheric boundary layer," J. Fluid Mech. **415**, 261 (2000).
[44] E. Bou-Zeid, M. Parlange, and C. Meneveau, "A scale-dependent Lagrangian dynamic model for large eddy simulation of complex turbulent flows," Phys. Fluids **17**, 025105 (2005).

This article is copyrighted as indicated in the article. Reuse of AIP content is subject to the terms at: http://scitation.aip.org/termsconditions. Downloaded to IP: 129.7.106.213 On: Tue, 19 Jan 2016 17:21:50

[45] W. Anderson and C. Meneveau, "A large-eddy simulation model for boundary-layer flow over surfaces with horizontally resolved but vertically unresolved roughness elements," Boundary Layer Meteorol. **137**, 397 (2010).
[46] P. P. Sullivan and J. McWilliams, "Dynamics of winds and currents coupled to surface waves," Annu. Rev. Fluid Mech. **42**, 19 (2010).
[47] D. Dommermuth and D. Yue, "A high-order spectral method for the study of nonlinear gravity waves," J. Fluid Mech. **184**, 267 (1987).
[48] C. Mei, M. Stiassnie, and D. Yue, *Theory and Applications of Ocean Surface Waves. 2. Nonlinear Aspects* (World Scientific, Singapore, 2005).
[49] V. Zakharov, "Stability of periodic wave of finite amplitude on the surface of a deep fluid," J. Appl. Mech. Tech. Phys. **9**(2), 190 (1968).
[50] X. Liu, S. Osher, and T. Chan, "Weighted essentially non-oscillatory schemes," J. Comput. Phys. **115**, 200 (1994).
[51] J. Kim and P. Moin, "Application of a fractional-step method to incompressible Navier-Stokes equations," J. Comput. Phys. **59**, 308 (1985).
[52] H. van der Vorst, "Bi-CGSTAB: A fast and smoothly converging variant of Bi-CG for the solution of nonsymmetric linear systems," SIAM J. Sci. Stat. Comput. **13**, 631 (1992).
[53] F. Xiao, "Implementations of multi-fluid hydrodynamic simulations on distributed memory computer with a fully parallelizable preconditioned Bi-CGSTAB method," Comput. Phys. Commun. **137**, 274 (2001).
[54] V. Yakhot and S. Orszag, "Renormalization group analysis of turbulence. I. Basic theory," J. Sci. Comput. **1**, 3 (1986).
[55] A. Yakhot, S. A. Orszag, V. Yakhot, and M. Israeli, "Renormalization group formulation of large-eddy simulations," J. Sci. Comput. **4**, 139 (1989).
[56] V. Yakhot, S. Orszag, S. Thangam, T. Gatski, and C. Speziale, "Development of turbulence models for shear flows by a double expansion technique," Phys. Fluids A **4**, 1510 (1992).
[57] Y. Watanabe, H. Saeki, and R. J. Hosking, "Three-dimensional vortex structures under breaking waves," J. Fluid Mech. **545**, 291 (2005).
[58] Y. Hu, X. Guo, X. Lu, Y. Liu, R. Dalrymple, and L. Shen, "Idealized numerical simulation of breaking water wave propagating over a viscous mud layer," Phys. Fluids **24**, 112104 (2012).
[59] H. Werner and H. Wengle, "Large-eddy simulation of turbulent flow over and around a cube in a plate channel," in *Proceedings of the 8th Symposium on Turbulent Shear Flows* (Springer, Berlin Heidelberg, Munich, Germany, 1991).
[60] D. Grigoriadis, J. Bartzis, and A. Goulas, "Efficient treatment of complex geometries for large eddy simulations of turbulent flows," Comput. Fluids **33**, 201 (2004).
[61] M. Donelan, A. Babanin, I. Young, and M. Banner, "Wave-follower field measurements of the wind-input spectral function. II. Parameterization of the wind input," J. Phys. Oceanogr. **36**, 1672 (2006).
[62] J. Miles, "Surface-wave generation revisited," J. Fluid Mech. **256**, 427 (1993).
[63] W. Plant, "A relationship between wind stress and wave slope," J. Geophys. Res. **87**, 1961, doi:10.1029/JC087iC03p01961 (1982).
[64] T. Larson and J. Wright, "Wind-generated gravity-capillary waves: Laborotary measurement of temporal growth rates using microwave backscatter," J. Fluid Mech. **70**, 417 (1975).
[65] J. Wu, E. Hsu, and R. Street, "Experimental study of nonlinear wave–wave interaction and white-cap dissipation of wind-generated waves," Dyn. Atmos. Oceans **3**, 55 (1979).
[66] R. Snyder, F. Dobson, J. Elliott, and R. Long, "Array measurements of atmospheric pressure fluctuations above surface gravity waves," J. Fluid Mech. **102**, 1 (1981).
[67] P. Janssen, "Quasi-linear theory of wind-wave generation applied to wave forecasting," J. Phys. Oceanogr. **21**, 1631 (1991).
[68] H. Lamb, *Hydrodynamics* (Dover Publications, New York, 1932).
[69] D. Vasilic-Melling, "Three-dimensional turbulent flow past rectangular bluff bodies," Ph.D. thesis, University of Imperial College London, (1977).
[70] D. Paterson and C. Apelt, "Simulation of flow past a cube in turbulent boundary layer," J. Wind Eng. Ind. Aerodyn. **35**, 149 (1990).
[71] K. E. Hanley, S. E. Belcher, and P. P. Sullivan, "A global climatology of wind-wave interaction," J. Phys. Oceanogr. **40**(6), 1263 (2010).
[72] P. P. Sullivan, L. Romero, J. C. McWilliams, and W. K. Melville, "Transient evolution of Langmuir turbulence in ocean boundary layers driven by hurricane winds and waves," J. Phys. Oceanogr. **42**, 1959 (2012).
[73] L. P. Van Roekel, B. Fox-Kemper, P. P. Sullivan, P. E. Hamlington, and S. R. Haney, "The form and orientation of Langmuir cells for misaligned winds and waves," J. Geophys. Res. **117**, CO5001, doi:10.1029/2011JC007516 (2012).

This article is copyrighted as indicated in the article. Reuse of AIP content is subject to the terms at: http://scitation.aip.org/termsconditions. Downloaded to IP: 129.7.106.213 On: Tue, 19 Jan 2016 17:21:50